Path Integral Monte Carlo Simulations of Quantum Wires

by

Jianheng Liu

A Dissertation Presented in Partial Fulfillment
of the Requirement for the Degree
Doctor of Philosophy

Approved November 2012 by the
Graduate Supervisory Committee:

John Shumway, Chair
Kevin Schmidt
Tingyong Chen
Hongbin Yu
Robert Ros

ARIZONA STATE UNIVERSITY

December 2012

ABSTRACT

One dimensional (1D) and quasi-one dimensional quantum wires have been a subject of both theoretical and experimental interest since 1990s and before. Phenomena such as the "0.7 structure" in the conductance leave many open questions. In this dissertation, I study the properties and the internal electron states of semiconductor quantum wires with the path integral Monte Carlo (PIMC) method. PIMC is a tool for simulating many-body quantum systems at finite temperature. Its ability to calculate thermodynamic properties and various correlation functions makes it an ideal tool in bridging experiments with theories.

A general study of the features interpreted by the Luttinger liquid theory and observed in experiments is first presented, showing the need for new PIMC calculations in this field. I calculate the DC conductance at finite temperature for both noninteracting and interacting electrons. The quantized conductance is identified in PIMC simulations without making the same approximation in the Luttinger model.

The low electron density regime is subject to strong interactions, since the kinetic energy decreases faster than the Coulomb interaction at low density. An electron state called the Wigner crystal has been proposed in this regime for quasi-1D wires. By using PIMC, I observe the zig-zag structure of the Wigner crystal. The quantum fluctuations suppress the long range correlations, making the order short-ranged. Spin correlations are calculated and used to evaluate the spin coupling strength in a zig-zag state. I also find that as the density increases, electrons undergo a structural phase transition to a dimer state, in which two electrons of opposite spins are coupled across the

two rows of the zig-zag. A phase diagram is sketched for a range of densities and transverse confinements.

The quantum point contact (QPC) is a typical realization of quantum wires. I study the QPC by explicitly simulating a system of electrons in and around a Timp potential (Timp, 1992). Localization of a single electron in the middle of the channel is observed at 5 K, as the split gate voltage increases. The DC conductance is calculated, which shows the effect of the Coulomb interaction. At 1 K and low electron density, a state similar to the Wigner crystal is found inside the channel.

ACKNOWLEDGEMENTS

I am grateful to Prof. John Shumway for his advising in five years. I have learned a lot not only from his horizon in physics, but also from his unique way of thinking and reasoning. His constant enthusiasm is always a good source of encouragement and inspiration. His optimism and amiability makes working with him a pleasant experience.

My second thanks goes to my parents. They maintain my connection to the people and the place I was familiar with, which offers me comfort. They do not know physics, but they always support the path I choose, allowing me to concentrate on my studies.

I would like to thank my colleague Lei Zhang who graduated one year ago, and my collaborator Zachary Estrada from the University of Illinois. Discussions with them turned out to be quite helpful in my study and enjoyable on their own.

Also, I want to thank the people who participate in the ALPS project (Algorithms and Libraries for Physics Simulations). I used their application in the study of spin correlation in the Wigner crystal.

Finally, I appreciate financial support from the National Science Foundation, grant no. NSF-OCI 1148502, during my final semester of graduate study.

TABLE OF CONTENTS

CHAPTER Page

CHAPTER Page

LIST OF TABLES

LIST OF FIGURES

Figure Page

Figure Page

Chapter 1

INTRODUCTION

At first glance, one dimensional (1D) physics may be simple and trivial in comparison to its two and three dimensional counterparts. Indeed, in the three dimensional world, particles can play a wide variety of tricks: they can rotate around a certain center; they can change their momentum greatly while change their energy slightly; in many cases, they are many, but they act one, etc. All of these devils—or angels depending on one's view—are gone, if they are restricted to the configuration of a straight line. They can now only move either left or right.

As particles move in 1D, they cannot avoid pushing or being pushed by their neighbors. Particles in one dimension are in a status of constantly interacting with each other. Due to the strong coupling between neighboring particles, a little local perturbation can be passed down, demanding the response of every particle. It means that the particle ensemble can no longer be considered as a single particle wandering around in a mean-field background potential. The motion is always collective, which gives birth to distinct features in one dimension and needs special treatment. In this dissertation, I investigate techniques for simulating electrons in and quasi-1D situations.

1.1 Introduction to Nanowires

The interest in one-dimensional (1D) systems in the last century was delayed until the development of new experimental techniques in the 1980s.

Thanks to the new growth methods, e.g. molecular beam epitaxy, physicists were able to build nano scale structures with few impurities. This led to the discovery of many interesting properties of 1D electron systems and made the study of nanowires a hot topic in 1990s.

Conductance is one of the most important properties of nanowires. The 1D ballistic transport of charge carriers results in quantized conductance. Modern growth methods are able to control impurities and defects in semiconductors, especially gallium arsenide. The greatly reduced probability of scattering extends the mean free path of electrons to microns. Therefore, the motion of electrons in a nanowire of tens of nanometers long is ballistic.

The typical conductance is shown in Fig. 1.1. The gate voltage controls the electron density. The more positive the gate voltage, the higher the electron density. As the density increases, the subbands are filled gradually. Each subband contributes a conductance quanta $2e^2/h$, so the conductance appears as plateaus in the unit of $2e^2/h$. At finite temperature as the experiments are conducted, thermal fluctuation softens the edges of the plateaus, connecting them with smooth ramps.

The interaction in 1D causes a peculiar conductance at low density, that is, the "0.7 structure" (Thomas *et al.*, 1996). In a quasi-1D wire, the smallest conductance becomes $0.7 \times 2e^2/h$ under certain conditions. This unusual plateau has been observed in different types of nano-structures (Cronenwett *et al.*, 2002; de Picciotto *et al.*, 2004; Crook *et al.*, 2006), which shows that it is a common characteristics in 1D quantum wires. In a typical wire, it exists up to 4.2 K and becomes weaker at very low temperatures. It vanishes in the presence of a magnetic field, indicating its relation with electron polariza-

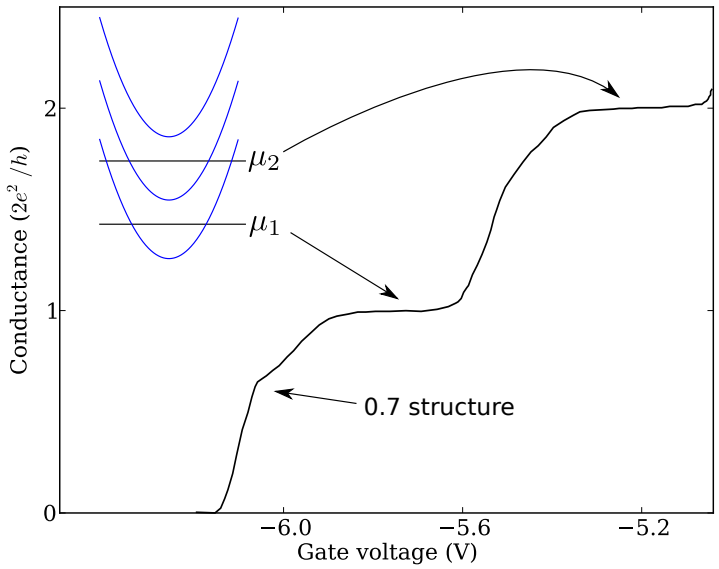

Figure 1.1: Typical quantized conductance and the "0.7 structure", from Thomas *et al.* (1998). As the gate voltage increases, the chemical potential increases and more and more subbands are filled. Each subband contributes $2e^2/h$ to the conductance, which explains the quantized conductance in experiments.

tion. It is still not fully understood despite of more than 10 years of research, exemplifying challenges in 1D physics.

In addition to the conductance, other aspects of 1D physics are also intriguing, such as the spin-charge separation. An electron has two spin states. The coupling between spins invokes spin waves, while the motion of electrons forms charge waves. In 1D, interactions change the speed of the two waves, so that they can be separated. The separation has been observed in experiments (Auslaender *et al.*, 2005). Spin-charge separation can be understood by the Luttinger liquid theory (Tomonaga, 1950; Luttinger, 1963; Deshpande *et al.*, 2010). More details of Luttinger liquid theory are given in Section 2.3.1.

Theoretical physicsts began studying the 1D electron system in the middle of last century, before experiments were feasible. The most successful model

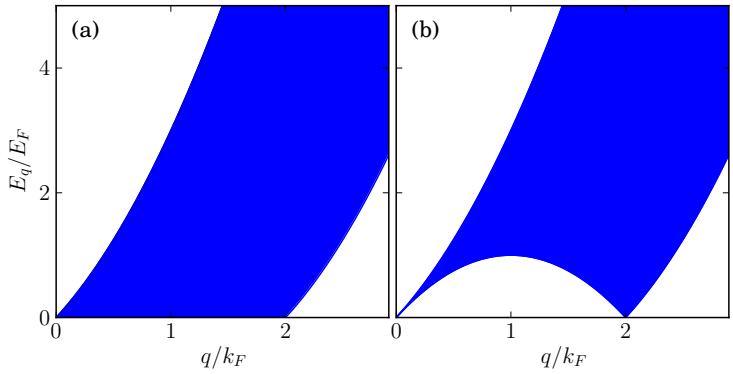

Figure 1.2: Shaded regions show allowed energy at given momenta of excitations of Fermi gas for (a) two or three dimensions and (b) one dimension.

was Luttinger liquid theory (LLT). We know that the motion of electrons in 1D is always collective, so many-body physics is inherent in 1D electron systems, and the elementary excitations are collective modes. LLT describes the low energy excitations of quantum wires. The key assumption in LLT is the linearization of the dispersion relations. In two or three dimensions, for a given excitation momentum $|\vec{q}| < 2k_F$, one can create excitations of vanishing energy by scattering an electron right below the Fermi surface to a state right above the Fermi surface, for some direction of $\vec{q}$. This freedom of direction is restricted to left and right in 1D, which leads to a significantly different momenta distribution for energy excitations, as is shown in Fig. 1.2.

If only the low energy excitations are concerned, the linearization of the Fermi surface is consistent with the excitation spectrum. Including Coulomb interactions, the LLT can be solved exactly by bosonization, showing that elementary excitations are collective modes acting as bosonic quasiparticles. In other words, the 1D interacting system of electrons can be mapped to a system of free bosons, as long as backscattering is forbidden.

LLT predicts several unique new phenomena as the consequence of the many-body physics, such as the power law dependence of the conductance on

temperature and the applied bias, and the separation between charge density wave and spin density wave. LLT has been applied to carbon nanotubes (Egger and Gogolin, 1997; Kane *et al.*, 1997), and the above predictions have been observed in experiments on metallic carbon nanotubes (Bockrath *et al.*, 1999; Yao *et al.*, 1999; Postma *et al.*, 2000), semiconductor nanowires (Auslaender *et al.*, 2000, 2002, 2005; Jompol *et al.*, 2009), and even self-organized atomic gold chains on the surface of Germanium (Blumenstein *et al.*, 2011). Meanwhile, deviations from LLT have also been observed (Auslaender *et al.*, 2002, 2005), triggering the development of a nonlinear theory beyond LLT (Imambekov and Glazman, 2009). However, the theory is still far from complete. On the other hand, LLT is only quantitatively valid in the high electron density regime, or in other words, the weak interacting regime. As the density decreases, the kinetic energy decreases as $\sim n^2$, while the Coulomb potential decreases as $\sim n$. When the density is below the inverse of the effective Bohr radius $a_B = \epsilon\hbar^2/m_e e^2$, the Coulomb potential dominates over the kinetic energy and the system enters the strong interaction domain, where non-perturbative theory has to be employed. This kind of theory is still a difficult challenge to physicists.

1.2 Application of Computer Simulations

The fast advancement of computer science has ushered in another way of attacking questions in physics. The solvable or integrable questions are only a small portion of the physics world. As for many complex systems, currently computer simulations are still the only way of obtaining the details. For example, density functional theory simulations of materials demonstrate the ability of computational physics. Beyond mean field theory, modern physics involves

more and more strongly interacting, or strongly correlated systems, such as the high T_c superconductivity and Wigner crystal phases. Analytic methods may be limited, while methods based on Monte Carlo algorithms are able to work straightforwardly. In this dissertation, I perform computer simulations using the path integral Monte Carlo method.

1.3 Path Integral Monte Carlo

Path integral Monte Carlo (PIMC) (Ceperley, 1995) is designed especially for simulating non-relativistic quantum many-body systems at finite temperature. The basic procedure in PIMC is making random walks (quantum trajectories of particles), then selecting from the walks according to the acceptance/rejection rate determined by the metropolis Monte Carlo algorithm. This procedure is repeated until the results converge.

PIMC uses random walks in configuration space to sample the density matrix. The density matrix, $\rho = \frac{1}{Z}e^{-\beta\hat{H}}$, in statistical physics can be formulated as a path integral over the configuration space (Feynman, 1972), Thus each particle in the configuration space is represented by a random walk or a path. By comparing this expression of the density matrix with the path integral formulation of quantum dynamics, people found that they could be related by the Wick rotation transformation $t \to t = -i\tau$, that is, the density matrix is an imaginary time path integral. The density matrix has an exponentially decaying factor $e^{-\beta H}$, so the integral converges well and is suitable to evaluate in computers. The imaginary time τ ranges from 0 to $\beta\hbar$, where $\beta = 1/kT$. Calculating $\mathrm{tr}(\rho)$ is equivalent to making closed paths. PIMC discretizes imaginary time into slices, and uses a bead on each slice to represent a particle at that instant. The kinetic energy can be considered as springs connecting

beads along a path. Time-independent many-body interactions, such as the Coulomb interaction, are imposed between beads on the same slice. Measuring physical properties is equivalent to evaluating averages over an ensemble of closed paths. The calculation of correlation functions at finite temperature is also straightforward, which is the main analysis tool which I apply in this dissertation. More details about PIMC can be found in Chapter 3.

1.4 Summary of my Results

By simulating a model in the regime of LLT and calculating the current-current correlation, I show that PIMC results are in good agreement with LLT in the high density regime. By making fewer approximations than LLT, PIMC calculations can be extended to lower densities.

To go beyond LLT, I study the quasi-1D quantum wires with very low electron densities. I find the zig-zag structure of the Wigner crystal and find that the long range correlation is diminished by quantum fluctuation. A look into the spin correlation in the zig-zag provides an estimation of the spin coupling strength. As the density increases, a dimer state emerges from the zig-zag.

The knowledge from the study of zig-zag is then applied to a simulation of a quantum point contact, which is a typical geometric configuration used in experiments. I first find the localization of single electron in the middle of the channel at 5 K by increasing the split gate voltage. The conductance is calculated by means of the method in Chapter 5. At 1 K and a lower electron density, the zig-zag state is found inside the channel between the split gates.

1.5 Outline of Dissertation

This dissertation is organized as follows: Chapter 2 discusses experimental and theoretical aspects of quantum wires. Chapter 3 describes the computational tool I use for the results, that is, the path integral Monte Carlo method. Chapter 4 provides the configurations of quantum wires and rings, on which my simulations are based. The next three chapters, 5, 6 and 7, are the main part of this dissertation, and show the results of my study on 1D electron systems. The conclusion is placed in Chapter 8. Supporting materials describing Coulomb interaction, density-density fluctuations and parallelism can be found in the Appendix.

Chapter 2

BACKGROUND

Thanks to the great efforts in the study of quantum wires, new techniques have been invented and new quantum wire physics has been discovered and understood in the past two decades. In this chapter, I review the realization of quantum wires in experiments and the techniques for measuring the transport properties. The theoretical approaches are discussed thereafter.

2.1 Physical Realization of Semiconductor Quantum Wires

There are several ways of realizing quantum wires in experiments, such as single wall carbon nanotubes, ultra-cold dilute atom chains, and a great variety of metallic and semiconducting nanostructures. In this dissertation, I focus on semiconductor quantum wires. The general idea of fabricating semiconductor quantum wires is to confine electrons from donors into a very thin layer, so that in the z-direction the electron gas is considered always in the ground state, and the layer becomes a 2D electron gas (2DEG). Then various metallic gates are used to shape the 2D electron gas into wires. To form the 2DEG, the most widely used structure is the GaAs/AlGaAs heterojunction.

2.1.1 GaAs/AlGaAs heterojunction with top gates.

One way to realize wires is to take advantage of the GaAs/AlGaAs heterostructure fabricated by molecular beam epitaxy (MBE) (Cho, 1971). AlGaAs has nearly the same lattice constant as GaAs, but the band gap is larger dependent on the concentration of Al. The fractional Al concentration is con-

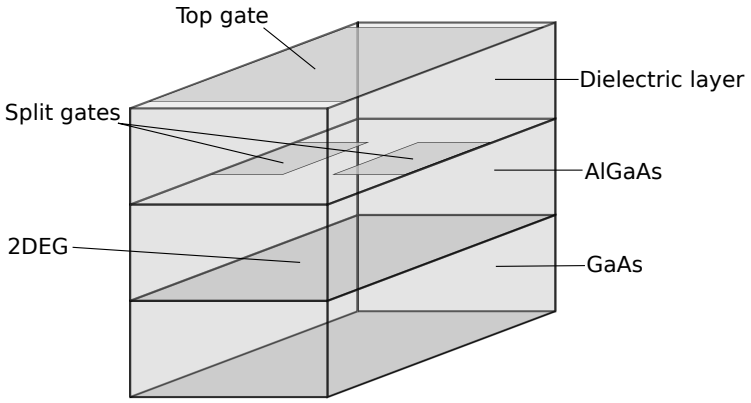

Figure 2.1: A quantum point contact formed at a GaAs/AlGaAs heterojunction. The quantum wire is the channel in the 2DEG defined in-between the two split gates.

trolled to be less than 0.4 so that the AlGaAs is still a direct band material. Then, at the interface between GaAs and AlGaAs, electrons are trapped in a V-shaped potential in the GaAs side. With a density around 10^{11} cm^{-2}, the Fermi wavelength of electrons is longer than the thickness of the electron gas, approximating a two-dimensional electron gas. The dopant is usually embedded by means of modulation doping, in order to keep the donor impurities far away from the heterointerface (Dingle *et al.*, 1978).

Once the 2DEG is formed, its shape can be controlled by top gates with negative voltage (Thornton *et al.*, 1986). To obtain one-dimensional electron gas (1DEG), the gates are made into the shape of split-gate point contacts, leaving a channel between them. Electrostatic repulsion causes electrons to be depleted from below the gates. The source and drain supplying bias voltage are made of common ohmic contacts deposited on two sides of the channel. Thus the electrons are driven through the channel and act like 1DEG. This is illustrated in Fig. 2.1.

2.1.2 GaAs/AlGaAs heterojunction with cleaved edge overgrowth.

The cleaved edge overgrowth method (Pfeiffer *et al.*, 1997), shown in Fig. 2.2 is another method of fabricating quantum wires out of quantum wells, which is convenient for studying the coupling between wires. It begins with an MBE and modulation doping process to obtain a GaAs layer sandwiched by AlGaAs along (001) direction. A long and narrow tungsten stripe stretched along (110) is then deposited on top of the [001] plane, acting as a top gate. With a negative voltage, this top gate depletes electrons below it, separates the 2DEG into the source and drain regions. It also helps define the quantum wire along the [110] edge of the GaAs layer.

Next, the [110] plane of the whole wafer is cleaved inside the MBE chamber and is overgrown immediately with a second modulation doping MBE process to form AlGaAs layer parallel to (001). This growth introduces extra electrons at the edge of the GaAs layer, which become 1DEG in direct contact with the 2DEG. A Ti-Au side gate is sometimes deposited over the overgrown [110] layer in order to control the electron density in the 1DEG. An appropriate voltage on the top gate then separates the 1DEG from the 2DEG and defines a quantum wire.

2.1.3 Other types of wires.

The idea of obtaining the 2DEG by heterostructures can also be used on other combinations of materials. The alloy $In_{0.53}Ga_{0.47}As$ has the same lattice constant as InP, while its band gap is smaller. Thus the same technique mentioned above can be used to fabricate InGaAs/InP quantum wires (Temkin *et al.*, 1987; Yoji Kunihashi and Nitta, 2009).

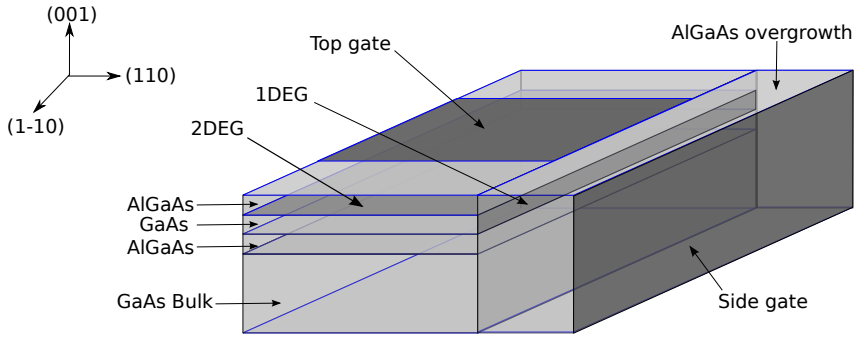

Figure 2.2: The GaAs/AlGaAs heterojunction with cleaved edge overgrowth. The top gate with negative voltage depletes the 2DEG below it and forms the quantum wire along the GaAs edge to the AlGaAs overgrowth. The side gate controls the density of electrons in the wire.

On the other hand, there are experiments based on self assembled InGaAs/GaAs quantum wires (Gréus *et al.*, 1992; Kunets *et al.*, 2012). Because of the lattice mismatch between InGaAs and GaAs, the growth is strain induced, and the strain field becomes the cause of potential well for electrons. It is a widely used technique for growing self-assembled InGaAs/GaAs quantum dots. By elongating quantum dots, quantum wires can be obtained. The difficulty here is that purity and uniformity of the wires is difficult to achieve. The measurement of conductance on a single sample of these wires is not easy, either. Therefore, they are rarely used to study unusual conductivity of quantum wires.

2.1.4 Erasable electrostatic lithography

The development of the erasable electrostatic lithography (EEL) provides another way of defining quantum wires based on the GaAs/AlGaAs heterostructure (Crook *et al.*, 2003, 2006). The sample is a GaAs/AlGaAs heterojunction 97 nm below the surface of the wafer. The junction serves as the 2DEG. A negatively biased scanning probe then draws negative charges on the surface. In order that the charges stay in place on the surface, the

whole experiment is conducted inside a dilution refrigerator cooled down to 20 mK. The surface charges act as top gates depleting the electrons below them, and define the shape of the desired quantum component. The advantage of EEL charges over epitaxial top gates is that the gates can be easily removed by a positively biased scanning probe. This flexibility enables experiments on different shapes of quantum components in a short period of time. The shapes can be further controlled by a scanning gate microscopy (SGM) probe 50 nm above the surface. Not only does the SGM probe image the shape of the quantum electronic device, but it also perturbs the local potential without changing the overall gating pattern. Therefore, the measurement with the probe at a special position can be considered as a measurement of a special quantum component.

To define quantum wires, a stripe of negative charges are drawn across the surface, separating the source and drain reservoirs to which ohmic contacts are connected. When the SGM probe with positive voltage moves to the center of the charges, a point contact structure is formed and a quantum wire is defined.

2.2 Transport Measurements on Quantum Wires

The most common measurement on quantum wires is the conductance, and most of the conductance is obtained by the two-terminal measurement. For ballistic transport in GaAs quantum wires, the conductance is determined by the number of transport channels in the wires. Each channel contributes $2e^2/h$ to the conductance according to the Landauer formula (Landauer, 1957, 1970). In experiments, the top gates control the density of electrons in the wire, while the split gates control the transverse confinement which defines the width of the wire. A two-terminal measurement measures the current and voltage between

the source and drain electrodes and gives the conductance as the ratio I/V. The measurement is usually conducted at a fixed split gate voltage, versus a decreasing top gate voltage that causes an increasing electron density inside the wire. As the electron density increases, more and more conducting channels are occupied. To study the change in the number of conducting channels, a low-frequency AC source-drain bias is applied, and differential conductance dI/dV is measured (Thornton *et al.*, 1986; van Wees *et al.*, 1991; Thomas *et al.*, 1996). DC conductance is also measured to understand the detailed structures in conductance (Kristensen *et al.*, 1998, 2000). Experiments have shown clear quantized conductance for high electron densities, as well as the peculiar "0.7 structure".

Four-terminal measurements are also applied to the study of conductance and interactions in quantum wires (de Picciotto *et al.*, 2001), in which two additional electrodes connected to the middle segment of the wire so that the voltage drop over an inner part of the wire can be measured. The conductance then becomes the ratio between the current and this inner voltage drop. The results confirm the ballistic transport in the quantum wire, and rule out the possibility of impurities as the cause of the "0.7" structure.

2.3 Theoretical Approaches to Quantum Wires

The quantization of conductance for ballistic transport of electrons can be easily understood from a single-electron model. Consider a quantum wire of length L at 0 K. Two metallic electrodes are attached, one to each end of the wire. A small bias V is applied to the electrodes, so that electrons move from left to right without scattering in the wire. The transport channels in the wire

are transverse modes, or subbands, in the wire with energy dispersion,

$$\epsilon_i = \epsilon_{i0} + \frac{\hbar^2 k^2}{2m^*}, \tag{2.1}$$

where ϵ_{i0} is the energy level of subband i, and m^* is the effective mass. The current can be expressed in Eq. (2.2),

$$I = \frac{e}{L} \sum_i \sum_k v_i(k) f(E), \tag{2.2}$$

where $v_i(k) = d\epsilon_i/dk$ is the group velocity of electrons in subband i near the Fermi level , $f(E)$ is the Fermi-Dirac distribution. The bias V causes the chemical potential difference between the electrodes, leading to electron flow from left to right. The $\sum_k$ can be converted into integral

$$\frac{1}{L} \sum_k \rightarrow \int \frac{1}{2\pi} \frac{1}{\frac{d\epsilon_i}{dk}} dE = \frac{1}{h} \int \frac{1}{v_i} dE \tag{2.3}$$

where the v_i conveniently cancels the group velocity in Eq. 2.2. If we use $M(E)$ to denote the density of subbands, μ_R and μ_L for the chemical potential of the left and right electrodes, and use Eq. 2.3, Eq. 2.2 can be converted into an integral,

$$I = \frac{2e}{h} \int_{\mu_R}^{\mu_L} f(E) M(E) dE. \tag{2.4}$$

where the factor 2 is due to the two spins of an electron. At 0 K, the chemical potential equals the Fermi energy, and the Fermi-Dirac distribution is a step function. With a small bias, $M(E)$ can be considered as a constant M. Thus, Eq. (2.4) can be simplified as in Eq. (2.5),

$$I = \frac{2e}{h} M(\mu_L - \mu_R). \tag{2.5}$$

On the other hand, we have Eq.(2.6),

$$\mu_R - \mu_L = eV. \tag{2.6}$$

Therefore, the conductance can be obtained as in Eq. (2.7),

$$G = \frac{dI}{dV} = \frac{2e^2}{h} M. \tag{2.7}$$

Thus each transport channel contributes $2e^2/h$ to the conductance.

To take into account possible scattering, the transmission probability can be added into the formula,

$$G = \frac{2e^2}{h} \sum_n T_n(E_F), \tag{2.8}$$

where $T_n(E_F)$ is the transmission probability of channel n near the Fermi energy.

2.3.1 Luttinger liquid theory

I have already mentioned in the introductory chapter that the one-dimensional (1D) electron systems inherently require many-body treatment, for which mean field theory is not a good approximation. If we restrict ourselves to the case of high electron density and low energy excitations, there is a successful model for 1D systems, that is, the Luttinger liquid theory (LLT).

As is briefly discussed in the last chapter, the idea of LLT is to linearize the Fermi surface. Here I follow the discussion in Giamarchi (2004). The Hamiltonian for spinless electrons is then (atomic units),

$$H_0 = \sum_{k,r} v_F(rk - k_F) c^\dagger_{k,r} c_{k,r}, \tag{2.9}$$

where $r = -1, +1$ denotes the left and right moving electrons repsectively, v_F is the Fermi velocity, $c_{k,r}$ is the annihilation operator of fermions following the anticommutation relation. The Coulomb interaction in general (omitting the $left$ and $right$ indices) is,

$$H_{int} = \frac{1}{2L} \sum_{k,k',q} V(q) c^\dagger_{k+q} c^\dagger_{k'-q} c_{k'} c_k. \tag{2.10}$$

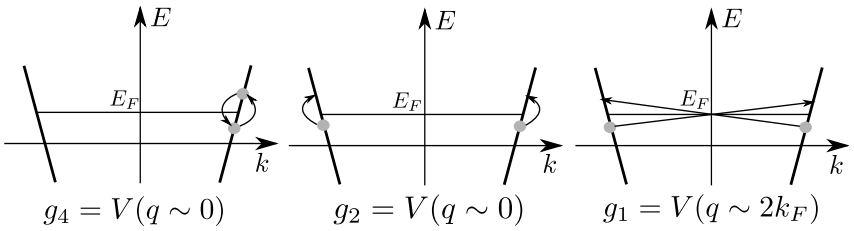

Figure 2.3: The three processes of low energy excitations for one-dimensional Coulomb interaction. Without considering spins, g_4 is from terms as $\rho_L(q)\rho_L(-q)$, g_2 and g_1 are from terms as $\rho_L(q)\rho_R(-q)$. They can be handled together with the kinetic term and solved completely. With spins, the only new term is g_1 process involving different spins $\sim \psi^\dagger_{L,\uparrow}\psi_{R,\uparrow}\psi^\dagger_{R,\downarrow}\psi_{L,\downarrow}$, which needs perturbative treatment.

As far as the low energy excitations are concerned, there are three processes as in Fig. (2.3) (notations follow Giamarchi (2004)). The parameter g_4 the interaction on one branch of the Fermi sea, g_2 denotes the forward scattering, and g_1 denotes the back scattering. The parameters g_1 and g_2 are equivalent unless the two electrons involved have different spins, in which case the chirality is changed and the theory cannot be exactly solved. Since we work with spinless electrons at present, we ignore g_1.

The density operator in momentum space can be defined as follows,

$$\rho_r(q) = \int dx\, e^{iqx}\rho_r(x) = \sum_k c^\dagger_{k+q,r}c_{k,r}. \tag{2.11}$$

The interaction term is (up to a chemical potential shift),

$$H_{int} = \frac{1}{2L}\sum_{q,r} g_2\rho_r(q)\rho_{-r}(-q) + g_4\rho_r(q)\rho_r(-q), \tag{2.12}$$

Define the boson operators,

$$\begin{aligned}
\phi(x) &= -(N_R+N_L)\frac{\pi x}{L} - \frac{i\pi}{L}\sum_{q\neq 0}\frac{1}{q}e^{-\alpha|q|/2-iqx}(\rho_R(q)+\rho_L(q)),\\
\theta(x) &= (N_R-N_L)\frac{\pi x}{L} + \frac{i\pi}{L}\sum_{q\neq 0}\frac{1}{q}e^{-\alpha|q|/2-iqx}(\rho_R(q)-\rho_L(q)),
\end{aligned} \tag{2.13}$$

where α is a short distance cutoff in order to ignore the large q behavior since we focus on the low energy excitations, N_R and N_L are the number of

electrons in each moving branch. The fermion operator can then be written as (Heidenreich *et al.*, 1980; Haldane, 1981),

$$\psi_r(x) = U_r \lim_{\alpha\to 0} \frac{1}{\sqrt{2\pi\alpha}} e^{ir(k_F - \pi/L)x} e^{-i(r\phi(x)-\theta(x))}, \tag{2.14}$$

where U_r is an non-Hermitian operator commuting with the boson operators and following the relation,

$$\begin{aligned} U_R^\dagger |N_R, N_L\rangle &= |N_R + 1, N_L\rangle, \\ U_L^\dagger |N_R, N_L\rangle &= |N_R, N_L + 1\rangle. \end{aligned} \tag{2.15}$$

It, together with the boson operators, provides a complete Hilbert space. Now the fermion operators has been expressed in terms of boson operators. The above transformation is named "bosonization". Define another boson operator

$$\Pi(x) = \frac{1}{\pi} \nabla\theta(x). \tag{2.16}$$

From Eq. (2.13), one can see that $\phi(x)$ and $\Pi(x))$ satisfy the canonical commutation relation,

$$[\phi_r(x_1), \Pi_s(x_2)] = i\delta_{rs}\delta(x_1 - x_2). \tag{2.17}$$

Using the new boson operators, the free fermion Hamiltonian Eq. (2.9) can be written as,

$$H_0 = \frac{1}{2\pi} \int dx\, v_F \left[(\pi\Pi(x))^2 + (\nabla\phi(x))^2 \right]. \tag{2.18}$$

The power of bosonization is that it can diagonalize the interaction simultaneously. First of all, when $L \to \infty$, from Eq. (2.13) we have,

$$\begin{aligned} \nabla\phi(x) &= -\pi \left[\rho_R(x) + \rho_L(x) \right], \\ \nabla\theta(x) &= \pi \left[\rho_R(x) - \rho_L(x) \right]. \end{aligned} \tag{2.19}$$

The fermion operator has to be separated into the left-moving and right-moving parts,

$$\psi(x) = \psi_L(x) + \psi_R(x). \tag{2.20}$$

Then the term concerning the g_4 process in Eq. (2.12) becomes,

$$\begin{aligned} \frac{g_4}{2}\psi_R^\dagger(x)\psi_R(x)\psi_R^\dagger(x)\psi_R(x) &= \frac{g_4}{2}\rho_R(x)\rho_R(x), \\ &= \frac{g_4}{2}\frac{1}{(2\pi)^2}(\nabla\phi - \nabla\theta)^2. \end{aligned} \tag{2.21}$$

The left-moving electrons can be expressed likewise, with the replacement $\phi - \theta \to \phi + \theta$. And the sum of the left and right moving terms are,

$$\frac{g_4}{(2\pi)^2}\int dx \left[(\nabla\phi)^2 + (\nabla\theta)^2\right]. \tag{2.22}$$

The term concerning the g_2 process becomes,

$$\begin{aligned} g_2\psi_R^\dagger(x)\psi_R(x)\psi_L^\dagger(x)\psi_L(x) &= g_2\rho_R(x)\rho_L(x), \\ &= \frac{g_2}{(2\pi)^2}(\nabla\phi - \nabla\theta)(\nabla\phi + \nabla\theta), \\ &= \frac{g_2}{(2\pi)^2}\left[(\nabla\phi)^2 - (\nabla\theta)^2)\right]. \end{aligned} \tag{2.23}$$

Eq. (2.22) and Eq. (2.23) can be merged into the boson representation of the free fermion Hamiltonian Eq. (2.18) as renormalization of the relative weights between ϕ and Π,

$$H = \frac{1}{2\pi}\int dx \left[uK(\pi\Pi(x))^2 + \frac{u}{K}(\nabla\phi(x))^2\right], \tag{2.24}$$

where,

$$\begin{aligned} uK &= v_F\left(1 + \frac{g_4}{2\pi v_F} - \frac{g_2}{2\pi v_F}\right), \\ \frac{u}{K} &= v_F\left(1 + \frac{g_4}{2\pi v_F} + \frac{g_2}{2\pi v_F}\right), \end{aligned} \tag{2.25}$$

and u has the unit of velocity, while K is dimensionless. Define $y = g/(\pi v_F)$, the expression of u and K is,

$$\begin{aligned} u &= v_F \left[\left(1 + \frac{y_4}{2}\right)^2 - \left(\frac{y_2}{2}\right)^2 \right]^{\frac{1}{2}}, \\ K &= \left(\frac{1 + y_4/2 - y_2/2}{1 + y_4/2 + y_2/2} \right)^{1/2}. \end{aligned} \tag{2.26}$$

Now we have mapped the 1D interacting fermion system to 1D free boson fields. The remarkable equivalence indicates the uniqueness that distinguishes 1D systems from its higher dimensional counterparts.

The above solution handles the spinless, or rather spin-polarized electrons. Taking spins into account means adding g_4 and g_2 terms involving electrons of different spin states,

$$H'_{int} = \frac{1}{2L} \sum_{q,r,s} g'_2 \rho_{r,s}(q) \rho_{-r,-s}(-q) + g'_4 \rho_{r,s}(q) \rho_{r,-s}(-q), \tag{2.27}$$

where $s = \uparrow, \downarrow$ is the spin index. The diagonalization is straightforward if we separate the charge and spin degrees of freedom,

$$\begin{aligned} \phi_\rho &= \frac{1}{\sqrt{2}}(\phi_\uparrow + \phi_\downarrow), \\ \phi_\sigma &= \frac{1}{\sqrt{2}}(\phi_\uparrow - \phi_\downarrow), \end{aligned} \tag{2.28}$$

and the same for θ. This transformation conserves the canonical commutation relation Eq. (2.17) between the charge operator and spin operator,

$$[\phi_\mu(x_1), \Pi_\nu(x_2)] = i\delta_{\mu\nu}\delta(x_1 - x_2), \tag{2.29}$$

where $\mu, \nu = \rho, \sigma$. Apply transformation Eq. (2.28) to the bosonization Eq. (2.14), we have,

$$\psi_{r,\sigma}(x) = U_{r,\sigma} \lim_{\alpha \to 0} \frac{1}{\sqrt{2\pi\alpha}} e^{ir(k_F - \pi/L)x} e^{-\frac{i}{\sqrt{2}}[r\phi_\rho(x) - \theta_\rho(x) + \sigma(r\phi_\sigma(x) - \theta_\sigma(x))]}. \tag{2.30}$$

Following the same procedures of bosonization for the spinless electrons, we can see that the kinetic term is separated into charge and spin parts $H_0 = H_\rho^0 + H_\sigma^0$, and so does the interaction Eq. (2.12) and Eq. (2.27). As a consequence, we obtain the same expression as in Eq. (2.24), only that the coefficients are renormalized with respect to charge and spin degrees of freedom,

$$\begin{aligned} H &= H_\rho + H_\sigma \\ &= \sum_\nu \frac{1}{2\pi} \int dx \left[u_\nu K_\nu (\pi \Pi_\nu(x))^2 + \frac{u_\nu}{K_\nu} (\nabla \phi_\nu(x))^2 \right], \end{aligned} \tag{2.31}$$

where $\nu = \rho, \sigma$, and,

$$\begin{aligned} u &= v_F \left[\left(1 + \frac{y_{4\nu}}{2}\right)^2 - \left(\frac{y_\nu}{2}\right)^2 \right]^{\frac{1}{2}}, \\ K &= \left(\frac{1 + y_{4\nu}/2 + y_\nu/2}{1 + y_{4\nu}/2 - y_\nu/2} \right)^{1/2}, \\ y_\nu &= \frac{g_\nu}{\pi v_F}. \end{aligned} \tag{2.32}$$

The g_1 interaction for 2 electrons of the same spins is identical to a g_2 process plus a swap of 2 electrons, that is, $g_1 = -g_2$. So this process can be incorporated into the above expression. Considering $g_4 = g_4'$, $g_2 = g_2'$ and $g_1 = g_1'$, we have $g_\rho = g_1 - 2g_2$, $g_\sigma = g_1$, $g_{4\sigma} = g_4$, $g_{4\sigma} = 0$.

The g_1 interaction between electrons of opposite spins needs a little care, by using Eq. (2.30), we have,

$$\begin{aligned} & g_1 \sum_s \psi_{L,s}^\dagger \psi_{R,s} \psi_{R,-s}^\dagger \psi_{L,-s}, \\ =& \frac{g_1}{(2\pi\alpha)^2} \sum_s e^{i(-2\phi_s(x))} e^{i(2\phi_{-s}(x))}, \\ =& \frac{2g_1}{(2\pi\alpha)^2} \cos(2\sqrt{2}\phi_\sigma(x)), \end{aligned} \tag{2.33}$$

This term has to be treated perturbatively. Nevertheless, it can be added to the spin degree of freedom in Eq. (2.31), and we have the complete expression

for the boson fields,

$$H = H_\rho + H_\sigma + \frac{2g_1}{(2\pi\alpha)^2}\int dx \cos(2\sqrt{2}\phi_\sigma(x)). \tag{2.34}$$

Eq. (2.34) shows the complete separation between the charge degree of freedom and the spin degree of freedom in the presence of interaction, and generally $u_\sigma \neq u_\rho$. This is the well-known spin-charge separation.

Since deviations from linear dispersion has been experimentally observed (Auslaender *et al.*, 2002), theories beyond LLT were proposed (Imambekov and Glazman, 2009). However, a complete description still needs a lot of work. On the other hand, the "0.7 structure" in the low density conductance has not been clearly understood. Theory for 1D electron systems is in need of new ideas. In the next chapter, we discuss how Path Integral Quantum Monte Carlo is well-suited to numerically address this problem.

Chapter 3

PATH INTEGRAL MONTE CARLO METHOD

In the recent three decades, the rising interest in strongly-correlated many-body systems has given birth to a wide suite of computational tools, to complement the difficult analytic studies. Among them, methods based on the metropolis Monte Carlo algorithm have become quite popular, due to their versatility and ease of use. Compared with the widely-used mean-field or single particle methods, they make very few approximations to the interactions. Compared with the exact diagonalization and the density matrix renormalization group methods, they scale much better as the size of the simulating system increases.

Path integral Monte Carlo (PIMC) is a particular kind of quantum Monte Carlo method, with some unique features. First of all, the path integral basis replaces the complexity of many-body wave functions with a useful analogy to classical systems. One does not have to design a trial wave functions out of a variety of considerations, as is the case in other quantum Monte Carlo (QMC) methods, such as variational Monte Carlo or diffusion Monte Carlo. The analogy to classical systems not only provides helpful insights, but also endows the complicated simulations with simple physical pictures, as most quantum systems have a classical limit. Secondly, owing to the mapping between the path integral formulation and statistical mechanics, PIMC directly provides finite temperature results, in contrast to most other numerical tools which study the ground-state quantum wavefunction at zero temperature. Finite temperature results are often favored by experiments which are always conducted under a

finite temperature. This is particularly important in extended metallic systems, like quantum wires, which do not have an energy gap. Finally, PIMC is able to evaluate the correlation functions straightforwardly, which can lead to a direct comparison with experimental results. On the other hand, like other numerical methods, PIMC has its drawbacks. For example, it cannot calculate the energy to a high accuracy. The main difficulty related to my research is that the correlation functions are calculated in imaginary time, so we obtain the imaginary frequency response. The analytic continuation from imaginary frequency to real frequency with the presence of noise is known to be very difficult. However, imaginary time correlation functions provide important insight into the physical systems, which turn out to be very useful. In this chapter, I first outline the basic algorithm of PIMC, then discuss in detail the special techniques I used in my study.

3.1 Statistical Mechanics and Imaginary Time Path Integral

Take the Schrödinger equation and do the imaginary time transform $t \to -i\tau$, we obtain the Bloch equation in atomic units, ($\hbar = m_e = e = 1$)

$$-\frac{\partial \rho}{\partial \tau} = H\rho. \tag{3.1}$$

The solution is the density matrix, which in the general form reads,

$$\rho = e^{-\int_0^\beta H d\tau}, \tag{3.2}$$

where $\beta = 1/kT$ and H is independent of time. Now consider a general interesting, many-body Hamiltonian,

$$H = T + V = -\frac{1}{2}\nabla^2 + V(\mathbf{R}), \tag{3.3}$$

where R represents the coordinates of all particles. Usually the kinetic term and the potential do not commute, so the Baker-Campbell-Hausdorff formula applies as we want to separate them,

$$e^{T+V+\frac{1}{2}[T,V]+\cdots} \approx e^T e^V. \tag{3.4}$$

However, we can divide the time integral in Eq. (3.2) into equal size of intervals $\Delta\tau = \beta/M$ where M is an integer, so that the integral can be approximated by a sum of M terms. If $\Delta\tau$ is small enough, we can drop the commutators since they are high order terms in $\Delta\tau$,

$$e^{\Delta\tau(T+V)} \approx e^{\Delta\tau T} e^{\Delta\tau V}, \tag{3.5}$$

which is justified by Trotter (Trotter, 1959) formula,

$$e^{-\beta(T+V)} = \lim_{M\to\infty} \left(e^{-\Delta\tau T} e^{-\Delta\tau V}\right)^M. \tag{3.6}$$

By inserting complete sets of position space states into each time interval, we arrive at the following formula as the beginning step of an N-body discrete path integral,

$$\begin{aligned} \langle R_0|\rho|R_M\rangle &= \rho(R_0, R_M; \beta) \\ &= \int dR_1 \ldots dR_{M-1} (4\pi\lambda\Delta\tau)^{-3NM/2} \\ &\quad \times \exp\left(-\sum_{m=1}^{M} \left[\frac{(R_{m-1} - R_m)^2}{4\lambda\Delta\tau} + \tau V(R_m)\right]\right), \end{aligned} \tag{3.7}$$

where R_m is the shorthand for $(r_1, r_2 \ldots, r_N)$, $\lambda = 1/2m$, and $\sqrt{\lambda\Delta\tau}$ is the largest diffusion distance for a particle in one move. Each time interval can be visualized as a link connecting two time slices. The collection of links from $\tau = 0$ to $\tau = \beta$ forms a path. Each particle is represented by a path. The kinetic energy can be considered as spring links. Interactions between

particles become interactions between ends of links on the same time slice. Statistical mechanics defines the expectation value of an observable $\mathcal{O}$ as $\langle\mathcal{O}\rangle = \mathrm{tr}(\rho\mathcal{O})$. In the language of PIMC, it means measuring $\mathcal{O}$ on each time slice and averaging over closed paths, for which $R_0 = R_M$. Correlation functions are estimated in the same manner.

The discretization works well if the action is a smooth function. As far as this dissertation is concerned, most actions comply with the requirement, except the Coulomb interaction, which is discussed in details in Appendix A.

In the simulation, we make the paths randomly walk through the position space. It is clear that PIMC only simulates equilibrium states. Therefore, it is essential to preserve ergodicity and detailed balance during random walks. The Metropolis algorithm guarantees that the random walks eventually result in equilibrium states and the trial moves are accepted according to the following formula,

$$A(s \to s') = \min\left[1, \frac{T(s' \to s)\pi(s')}{T(s \to s')\pi(s)}\right], \tag{3.8}$$

where $T(s \to s')$ is the transition rate from state s to state s', and $\pi(s)$ is the probability of the system in state s.

So far, we have established PIMC for semi-classical particles, since particles are distinguishable. With regard to a pure classical system, each particle is just a dot instead of a path, for $\hbar = 0$. In order to simulate bosons and fermions, we need to take into account of the indistinguishability of particles.

3.2 Fermi Statistics and the Fixed Node Approximation

To include the permutation between identical particles, we write Eq. (3.7) as,

$$\rho(R_0, R_M; \beta) = \frac{1}{N!} \sum_{\mathcal{P}} (\pm 1)^{\mathcal{P}} \int dR_1 \dots dR_{M-1} \rho(\mathcal{P}R_0, R_1; \tau) \dots \rho(R_{M-1}, R_M; \tau). \tag{3.9}$$

The $(+1)^{\mathcal{P}}$ denotes Bose statistics and the $(-1)^{\mathcal{P}}$ denotes Fermi statistics. Directly calculating each permutation term in Eq. (3.9) is very inefficient, for the computational amount increases as $N!$. Instead, one samples the permutation with random walk.

As a discreet move, the transition rate of a permutation can be determined by the heat bath rule,

$$T(s \to s') = \frac{\pi(s')}{\sum_{s'' \in \mathcal{N}(s)} \pi(s'')}, \tag{3.10}$$

$\mathcal{N}(s)$ is the collection of states near s. In Eq. 3.7, the potential does not change under permutations. So permutations only affect the kinetic term, which can be easily calculated. At the beginning of a simulation, we build up a table of probabilities of all permutations, then make random walks through the table to construct permutations involving a certain number of particles. The acceptance rate of the picked permutation is weighted based on Eq. (3.10),

$$A(s \to s') = \min \left(1, \ \frac{\sum_{s'' \in \mathcal{N}(s)} \pi(s'')}{\sum_{s'' \in \mathcal{N}(s')} \pi(s'')} \right), \tag{3.11}$$

That implements the Bose statistics.

The above permutation sampling can also be applied to fermions. However, because of the (-1) in front of every odd permutation, a large portion of the terms in Eq. (3.9) either cancel out or contribute only a little to the sum. The

CPU time on those terms are wasted, causing a slow convergence. In other words, the state space of fermions is much smaller than that of semi-classical particles or bosons. Trial moves outside the fermion state space are a waste of time. So a straightforward permutation sampling for fermions only works for small systems. In order to simulate a large number of fermions, one needs a method to effectively identify terms of non-zero contribution in series Eq. (3.9). The fixed node approximation is such a method.

Examining the Bloch equation Eq. (3.1), we can see that locations satisfying $\rho = 0$ are the fixed points in position space. They are hyperplanes dividing the 3N-dimensional space into unconnected regions, through which no paths can pass. They are called the fermion nodes. They do not exist in semi-classical or bosonic simulations, because we are only concerned about closed paths and the diagonal terms of a density matrix are always positive. If we know exactly the fermion nodes, we can use them as boundary conditions and solve Eq. (3.1) to get the exact density matrix for fermions. For PIMC, we can restrict paths inside the area between nodes and perform bosonic moves to the paths, the result is an exact fermionic simulation. To check if the nodes are crossed, what we need is a reference location R_*. Suppose we want to check if a bead $R_i(\tau)$ crosses the nodes, we choose $R_* = R_i(\tau + \beta/2)$ and calculate $\det[\rho(R_i, R_*; \beta/2)]$. If the determinant changes sign, the nodes are crossed and the move is rejected. We cannot choose more reference points, because that would introduce the sign problem back. Since $R_i(\tau)$ can be on any time slice, we preserve the translational symmetry in imaginary time. It is an efficient sampling method for fermions and is feasible for large systems.

The fixed nodes are determined by the Hamiltonian. In the presence of complex interactions, obtaining the fixed nodes is not much easier than solving

the Bloch equation. So we can only approximate the exact fixed nodes. The exception is one-dimensional systems, where we simple forbid permutation. As far as quantum wires are concerned, we used the exact density matrix $\rho(\vec{r}, \vec{r'}; \tau)$ of Hamiltonian $H = \mathbf{p}^2/(2m) + (1/2)m\omega_0^2 y^2$ to define the nodes,

$$\frac{1}{N} \det[\rho(\mathbf{r}_i, \mathbf{r}_j; \tau)] = 0. \tag{3.12}$$

The effect of fixed node approximation on correlation functions is studied in Appendix B.

3.3 Sampling Methods

Since the ergodicity and Metropolis algorithm have taken care of convergence, the major concern on designing a sampling method is the efficiency, or in other words, the convergence rate given a certain amount of time. One approach to improve efficiency is the multilevel sampling.

3.3.1 Multilevel sampling

I have already shown that each particle is represented by a path, and each path is comprised of beads linked by springs. External potentials exert on single beads, whereas particle interactions exist between beads on the same time slice. Because of the Gaussian distribution of the spring action, each bead can not move much farther than a thermal de Broglie wavelength $\sqrt{\lambda\Delta\tau}$. The pair interactions about which I am concerned, such as the Coulomb interaction, shorten the the displacement even more. If each time only one bead is moved, the time for the path to diffuse throughout the whole space could be very long in order to achieve ergodicity. So it is necessary to move multiple beads at the same time. The multilevel sampling selects the moving beads in a

generally efficient way. Let's take a path with two fixed ends (R_i, R_{i+m})—the subscript is the slice index—as an example. The multilevel sampling first tries moving the middle bead $R_{i+m/2}$. This bead can be moved furthest, because the thermal wavelength for it is $\sqrt{\lambda\Delta\tau m/2}$. So the acceptance rate for this move is generally the lowest. If the move is accepted, the sampling then takes the bead as fixed and moves the next level of beads which are in-between the 3 fixed ends, that is $R_{i+m/4}$ and $R_{i+3m/4}$. The 2 beads usually gain a higher acceptance rate. If the moves are accepted, the sampling continues to bisect the resulting links until it reaches the level we set. If for some level the move is rejected, the sampling starts over. The total acceptance rate is the product of the rate of each level. Since the sampling tries the bead of lowest acceptance rate first, it avoids the possible waste of time on beads of high acceptance rate which finally get rejected.

3.3.2 The worm algorithm

The worm algorithm (Massimo Boninsegni and Svistunov, 2006; Boninsegni and Svistunov, 2006) is able to sample the off diagonal terms in the density matrix. In other words, it samples the grand canonical ensemble. It is based on the same path integral expression Eq. (3.7), and the metropolis Monte Carlo algorithm Eq. (3.8), while it introduces moves that open or close the existing paths, and moves that generate or remove open paths in vacuum. Its swap method is able to generating long permutations easily, making it especially efficient in calculating properties concerning the winding of paths, such as the superfluidity.

However, I did not use worm algorithm in my research for two reasons. First of all, there are little applications of the worm algorithm on Fermionic

systems, due to the difficulty of incorporating the Fermi-Dirac statistics efficiently. Since I am concerned about electron systems, the worm algorithm does not help. Secondly, my interest is in the low electron density regime, where electrons are far apart. The Pauli exclusion and the strong Coulomb repulsion significantly reduce the probability of long permutations, making the ability of sampling the winding paths unimportant.

Therefore, instead of implementing the worm algorithm, I introduced some other sampling methods for our closed paths algorithm.

3.3.3 Other sampling methods for my research

Depending on the specific system, more sampling methods are applied. In my simulation of quantum wires, the electron density is so low that multilevel sampling still takes a long time to diffuse the electrons. So we implement displacement moves, which attempt to shift an entire path of one or more particles by a uniform displacement. Since all the beads on a path are shifted, the acceptance rate is determined by the action difference of all the beads on that path, and is usually adjusted to 50% so that the error bars drop quickly. For particles involved in permutations, their displace moves are always rejected. We can move more than one particle at the same time, but the acceptance rate drops quickly. In my simulation for zig-zag state, to keep the 50% rate, the largest displacement for 1-particle displace moves is about 1/3 of the average electron spacing, while for 2-particle moves, the largest displacement drops to about 1/6 of the spacing.

Quantum wires possess translational symmetry, which leads to uniform distribution of electrons along the wires. With the above sampling methods, we find that it is difficult for the density of electrons to become uniform.

To speed up the distribution of electrons along the wire, we apply a special displace move to all the electrons at the same time. The displacement of particle i is given by a sine function,

$$\mathbf{d}_i = \mathbf{A}\sin(\mathbf{k}\cdot\mathbf{r}_i + \varphi). \tag{3.13}$$

So some particles are compressed towards each other, whereas others depart away. Because of the periodic boundary condition, k is chosen to be $2\pi n/L$ where n is an integer. I randomize the phase φ during simulations so that the position of each electron can be stretched and compressed. The amplitude $\mathbf{A}$ is adjusted for each specific system to give an acceptance rate near 50%.

The use of a sine function raises two issues. First of all, sine is not the inverse function of itself, which means it breaks the detailed balance if we don't calculate the inverse moves explicitly. Secondly, sampling from a sine function with heat bath rule must take into account the change in transition probability which is 100% for sampling from a uniform distribution.

We follow Maggs (2006) to handle the issues. The inverse function of sine is calculated explicitly by Newton iteration as the function for backward moves. The forward moves and backward moves are chosen with 50% probability respectively. The neighborhood of the forward moves is $\pi(\mathbf{r})d\mathbf{r}$, and the neighborhood of the backward moves is now $\pi(\mathbf{r}')d\mathbf{r}J_d$ where J_d is the Jacobian of the displacement Eq. (3.13). The acceptance rate Eq. (3.8) becomes,

$$A(s \to s') = \min\left[1, \frac{T(s' \to s)\pi(s')}{T(s \to s')\pi(s)J_s}\right]. \tag{3.14}$$

Thus the detailed balance is conserved.

Since here all the particles are moved, the acceptance rate drops quickly as the amplitude increases. So the amplitude in Eq. (3.13) is usually less than

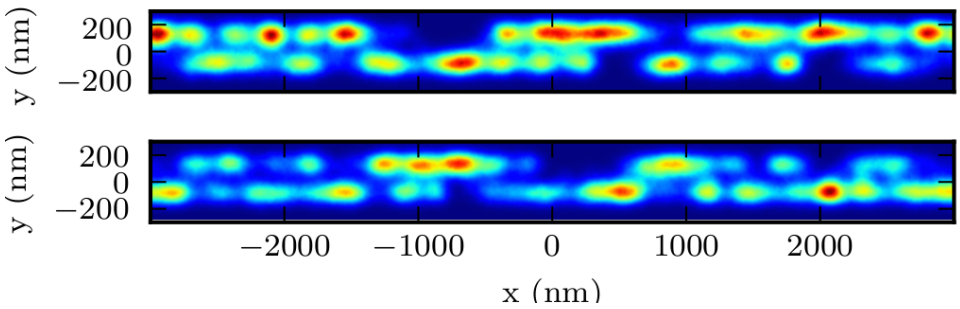

Figure 3.1: Density of spin-up and spin-down electrons respectively without the swap moves. The result is obtained after one week running on a quad-core CPU. Clearly it is not convergent, which shows that improvements such as swap moves are necessary to obtain converged results in a reasonable time. The physical result with swap moves is shown in Fig. 3.2.

the average particle spacing. I find that to reach 50% acceptance rate, the amplitude is about 1/5 of the average electron spacing with largest $\mathbf{k}$.

There is another issue concerning ergodicity when there are both spin-up and spin-down electrons in the simulation of quantum wires. Combining all the above sampling methods, I get the density shown in Fig. 3.1. The density does not change much no matter how long I run the simulation, which breaks the translational symmetry and raises serious concerns about ergodicity. The reason is in quasi-1D quantum wires with strong Coulomb interaction, it is very hard for electrons to diffuse along the wire. The collective moves shift electrons back and forth, but fail to diffuse different spin species towards each other. The multilevel sampling can do that, but takes a very long time. So the system is locked in a density distribution, meaning the system is not sampled well. A new move that can effectively diffuse two spin species is needed.

I therefore introduce the move that swaps a spin-up electron and a spin-down electron. This move is costly in CPU time, because I need to check the node crossing for each spin species separately. Furthermore, since there are no nodes between spin-up and spin-down electrons, the paths of distinguish-

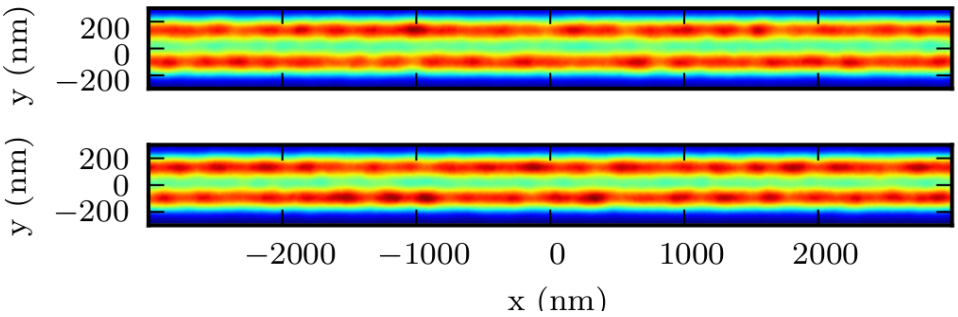

Figure 3.2: Density of spin-up and spin-down electrons respectively with the swap moves. The result is obtained after several hours running on a single processor.

able particles can get close or even overlap. Thus, after a spin-up electron is replaced by a spin-down electron, it is highly possible that the path of the new electron touches the paths of nearby spin-down electrons, causing node crossing and rejection. So in the simulation, the acceptance rate is usually less than 10%. As the density increases, the rate drops quickly. In order to make sure the two spin species diffuse sufficiently, I employ a large number of swap moves and check that this has restored the translational symmetry; the resulting density is shown in Fig. 3.2.

3.3.4 Spin-Flip sampling

So far, we have been dealing with systems of a fixed number of spin-up and spin-down electrons, that is systems of constant magnetization. In other quantum Monte Carlo method, spin is treated together with wavefunction explicitly. But in PIMC, spin is in a state space different from the position space and has no classical analogy. It is somewhat difficult to add spin to a polymer-like path and include it in interactions. With a fixed-node method, nodes for spin-up electrons and spin-down electrons are calculated by determinant of different Slater matrices. Flipping a spin causes both matrices change rank,

leading to technical problems for implementation. It is also difficult for PIMC to deal with arbitrary spin rotation, because of Berry's phases.

Therefore, we assume that spin is quantized along z-axis and sample spin flips. Since we are not concerned about interactions that break the global rotational symmetry, such as nonuniform magnetic fields, spin-flip sampling is valid. When a spin is flipped, the action difference is only changed by the fixed-node terms. The fixed node action at the nodes is infinity. When a particle is near a node at $R = 0$, the nodal action is determined by the distance between the particle and the node,

$$S(R_t, R_{t+\tau}) = \ln[\rho(R_t, R_{t+\tau}) - \rho(R_t, -R_{t+\tau})], \tag{3.15}$$

where $-R_{t+\tau}$ represents a many-body configuration with a node crossed. We use only one Slater determinant to check node crossing for both spin-up and spin-down electrons. Since the number of electrons is constant, the size of the Slater matrix is constant. The matrix elements between electrons of different spins are zero. So the matrix can be diagonalized into 2 blocks—one is the original matrix for spin-up electrons and one is for spin-down electrons. If determinant of either one of the blocks changes sign, the nodes are crossed. Because of the nodal action Eq. (3.15) and the flipping of one spin per each time, the situation that 2 determinants change sign at the same time hardly takes place.

The amount of computation is equal to the computation of the same number of spin-polarized electrons. But the gain is significant. PIMC only simulates canonical ensemble with a certain magnetization Z_m, now we are able to simulate grand canonical ensemble of spins, that is $Z = \sum_m Z_m$. The spin-flip sampling is more flexible and efficient than the swap moves, for it includes

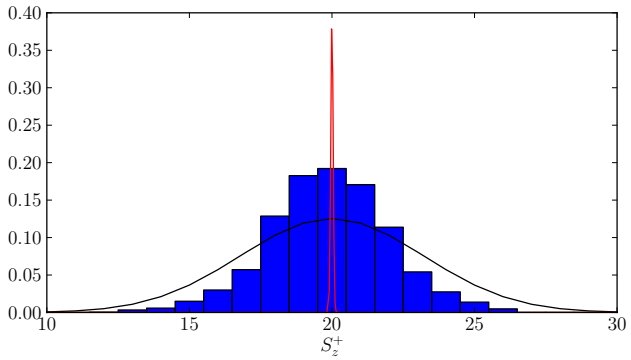

Figure 3.3: The distribution of up spins in a zig-zag simulation of 40 electrons (details in Chapter 6). The smooth curve is the distribution for free spins, the sharp curve is the spin distribution for 1D free electron gas (rescaled by a factor of 0.33). The free spin case can be considered as electrons infinitely apart from each other, the simulation including Pauli exclusion and the Coulomb repulsion brings electrons closer, and the absence of Coulomb repulsion allows even smaller separation between electrons. The increasing correlation with decreasing separation causes less susceptibility. The highest probability at $S_z^+ = 20$ indicates the absence of spontaneous magnetization. The small asymmetry just needs more CPU hours to equilibrate.

more kinds of moves. It also helps reduce the autocorrelation. So far as the zig-zag simulation is concerned, my test shows that a simulation which previously took one week now only takes one day to converge. A typical result is shown in Fig. 3.3. The spin-flip sampling also opens a door to more interactions we can study. For example, we can now study Zeeman splitting in quantum dots.

3.4 Estimators

Estimators approximate the measurements of physical properties based on the paths. The evaluation of static thermodynamic properties is straightforward. We simply measure the properties at each slice, then average them over the paths. The error is the standard deviation of the mean of the measurements. The static correlation function, such as the pair correlation function, can be evaluated likewise.

Since the measurements in quantum Monte Carlo are often correlated, standard deviation of the mean underestimates the error. To reduce the autocorrelation, the blocking method is used (Nightingale and Umrigar, 1999). The method averages over the non-overlapping pairs of measurements to generate new series of measurements, based on which the standard deviation of the mean is evaluated as the error. The autocorrelation is reduced further after each averaging, and the measurements approach the true value with more accurate error bar.

With regard to dynamic properties, e.g. the current-current correlation function, we first measure the functions on each slice, then Fourier transform them into frequency domain. Since PIMC is define in imaginary time, the resulting dynamic correlation functions are also defined in imaginary time. In principle, an analytic continuation from imaginary time to real time gives the results in direct comparison to experimental data. However, the existence of noise/error sets a formidable obstacle between the imaginary domain and its real counterpart. The continuation is usually unfeasible. Nevertheless, the dynamic estimators provide insights into properties such as conductance.

Chapter 4

SIMULATIONS OF MODEL WIRES

4.1 One-dimensional Wires

The most straightforward way to study a wire is a simulation in exactly one dimension (1D). In this case, the strong repulsion due to the Coulomb interaction keeps particles apart and forbids permutation. As a consequence, the 1D boson gas, also known as the Tonks-Girardeau gas (Girardeau, 1960; Lieb and Liniger, 1963), behaves the same as the 1D electron gas. Also spontaneous spin polarization is forbidden according to the Lieb-Mattis theorem (Lieb and Mattis, 1962). Because of the strong quantum fluctuations, any electron structures, such as the Wigner crystal, can not exist. PIMC simulations in 1D do not provide many insights beyond those gleaned from theories or other simulation techniques.

However, strictly 1D simulations are good test cases to check the PIMC simulations. Without interactions, a PIMC simulation for electrons in 1D is exact, because the nodes for the fixed node method are known to be in-between every pair of electrons. I have run some simulations in 1D for non-interacting electrons and studied the density-density correlation functions. The results are shown in Appendix B and fit well with theoretical predictions. Since my research interest is in the strong interaction regime and the spin correlation, I concentrate on quasi-1D quantum wires.

4.2 Quasi-1D Wires

A quasi-1D model shares more resemblance with experiments and enables more interesting physics that is not yet understood in theory. It is essentially a two-dimensional simulation with a transverse parabolic confinement defining the quantum wire. The following model of a quasi-1D quantum wire is used for the study in Chapter 5 and Chapter 6.

I use an effective mass Hamiltonian in two dimensions,

$$H = \sum_{i}^{N} \frac{p_i^2}{2m_i^*} + \sum_{i}^{N} V(\mathbf{r}_i) + \sum_{i \neq j} v(\mathbf{r}_i, \mathbf{r}_j). \tag{4.1}$$

Since GaAs is the most widely used material for quantum wires, I let $m_i^* = 0.0667 m_e$. The wire is laid along x direction and a parabolic confinement is imposed along y direction, that is, $V(\mathbf{r}_i) = 1/2 m_i^* \omega_0^2 y_i^2$. The only inter-particle interaction is the Coulomb interaction. In experiments, there is typically a metal layer below the wire, providing free electrons. The layer causes screening image charges at a distance d below the wire. Thus the last term in Eq. 4.1 is the Coulomb interaction with screening charge,

$$v(\mathbf{r}_i, \mathbf{r}_j) = \frac{e^2}{\epsilon |\mathbf{r}_i - \mathbf{r}_j|} - \frac{e^2}{\epsilon \sqrt{|\mathbf{r}_i - \mathbf{r}_j|^2 + d^2}}, \tag{4.2}$$

where $\epsilon = 12$ denotes the dielectric constant in GaAs.

4.3 Ring Geometry with Constriction

From a theoretical point of view, quantum wires with periodic boundary condition can be modeled as quantum rings. The analogy is well established so long as there are no interactions associated with the specific topology of the system. One example of such an interaction is a magnetic field perpendicular to the plane of the ring. Since we are interested in the strong Coulomb interaction

in the low electron density regime and the crossover from the low density regime to the high density regime, the ring model works as good as a wire.

The transition between an electron liquid to a Wigner crystal has been the subject of both experimental and theoretical research (Steinberg *et al.*, 2006; Jamei *et al.*, 2005). Due to the strong interaction in the Wigner crystal regime, computational methods beyond mean field approximation have been applied (Casula *et al.*, 2006; Ghosal *et al.*, 2007; Güçlü *et al.*, 2008; Shulenburger *et al.*, 2008; Güçlü *et al.*, 2009). In the low electron density regime of a quasi-1D system, localized electron states were observed, and the pair correlation function indicated the formation of a Wigner crystal of electrons. Here I use PIMC to study the inhomogeneous 1D electron gas. PIMC has the convenience of not constructing the wave function of specific properties. It is thus suitable for the simulation of this structural transition.

4.3.1 The model

I follow Güçlü *et al.* (2009) to build up the Hamiltonian for the ring,

$$\begin{aligned} H = & \sum_{i}^{N} \frac{\mathbf{p_i}^2}{2m^*} + \frac{1}{2}\sum_{i}^{N} m^*\omega_0^2(r_i - r_0)^2 + \sum_{i<j}^{N} \frac{1}{\epsilon|\mathbf{r}_i - \mathbf{r}_j|} \\ & + V_g\{\tanh[s(\theta_i + \theta_0)] - \tanh[s(\theta_i - \theta_0)]\}, \end{aligned} \tag{4.3}$$

where m^* is the effective mass of electrons. Since I deal with GaAs quantum rings, $m^* = 0.0667m_e$ and $\epsilon = 12$. The second term is a radian parabolic confinement as the definition of the ring, I set $\omega = 7.14$ meV. The last term is the potential of a top gate. This function has a smooth edge as can be seen in Fig. 4.1, so that its implementation in our PIMC code is straightforward. This top gate excludes electrons from the specified segment of the ring, and creates a low density regime. In my simulations, I set $s = 4.0$ and $\theta_0 = 1.5$.

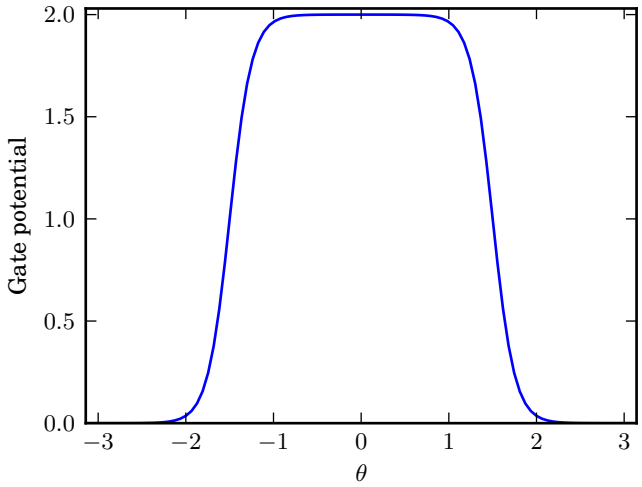

Figure 4.1: The gate potential for the ring. Parameters have been chosen to be the same as those in my simulations.

The periodic boundary condition is imposed by default. In order to avoid the undesired interaction between supercells, I make a large supercell of 1.4 micron $\times$ 1.4 micron and make the radius of the ring 100 nm. With regard to the Coulomb interaction, I put a screening layer 50 nm below the ring which generates image charge 100 nm below the ring. It is a mimic of typical experimental setup. The screening of the long range tail of Coulomb interaction is not important here, since the ring is an isolated structure.

The fermion sign problem is handled by the fixed node approximation, I apply the nodes of free fermions. I simulate 16 spin-polarized electrons. Considering the radius of the ring is 100 nm, the average particle spacing is about 40 nm, giving $r_s \approx 4$ a.u.. In this regime of strong repulsive interaction, one-dimensional bosons behave like fermions, for the interaction keeps particles away from the nodes.

My results are shown in Fig. 4.2. I run all the simulations at 0.5 K so that the electrons only occupy the first subband. As the gate voltage decreases,

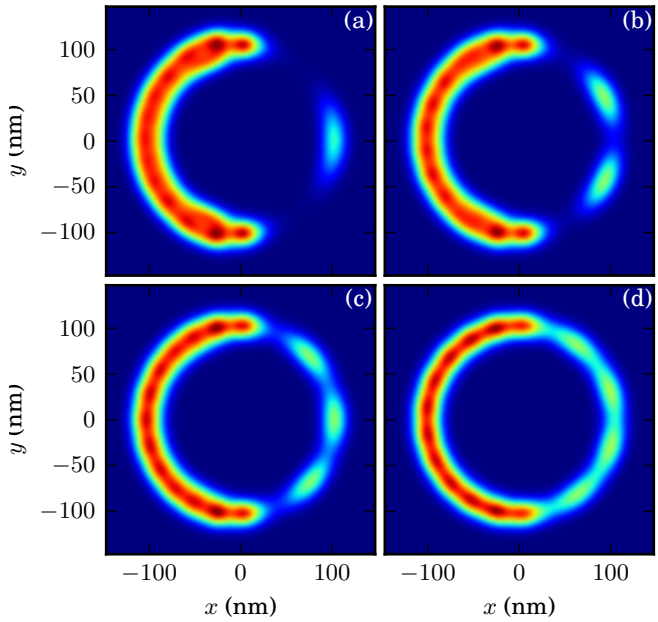

Figure 4.2: Different densities of electrons inside the gate. The temperature is 0.5 K, the total number of electrons is 16, the gate voltage is (a) -10 meV; (b) -9 meV; (c) -8 meV; (d) -6.5 meV. It is clear that as the gate potential increases, the number of localized electrons decreases.

electrons localized inside the gate area increases. My results share similar features as Güçlü *et al.* (2009) in the low density regime where electrons are individually localized and separated from the high density regime by a large gap. However, I observe different phenomena. First of all, with half of their electron density, I allow stronger interaction in my model. And the localization inside the gate area is also enhanced by the spin polarization. Therefore, at the same gate voltage, there is less localization in the low density regime, and it increases more slowly as the gate voltage decreases. Secondly, even for a smooth potential step, the connection between the crystal and liquid phases are not smooth. we can see a clear density peak at the connection. It is possibly due to the Coulomb blockade effect under strong interaction. This is clearest in the case of only one localized electron. Finally, the thermal fluctuation shows its effect. Unlike the quantum Monte Carlo method at zero

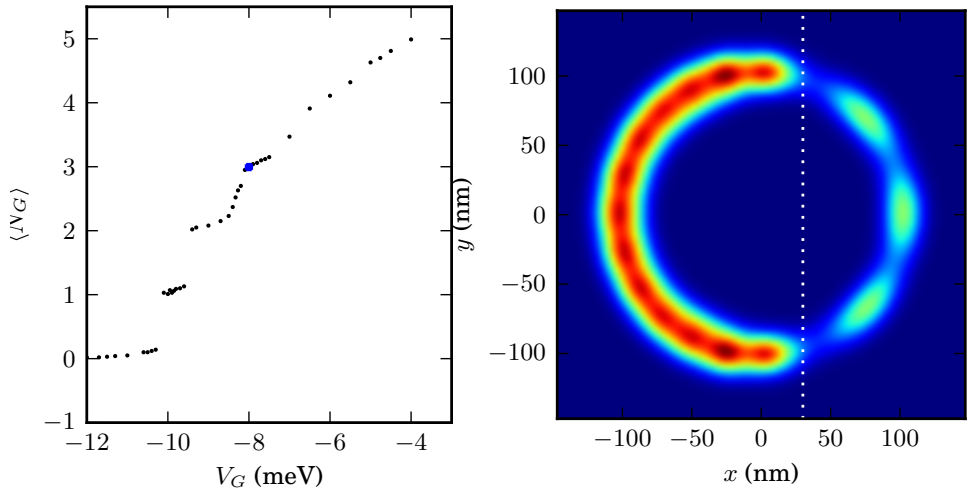

Figure 4.3: Dependence of the number of localized electrons on the gate potential. I calculate the number of localized electrons by summing up the density to the left of the white dashed line on the right plot.

temperature, the density of electrons in the low-density regime spreads out, softening the gap between the two regimes.

Fig. 4.3 shows a summary of my results. We can see the quantization of localization inside the gate potential as a function of the gate voltage. The plateaus are not strictly horizontal because the method of counting electrons includes some error if the density in the gap between the two phases is not exactly zero. The effect of fluctuations is more manifest on the plot. As the gate potential decreases, the number of electrons increases inside the gate area, causing an increase in quantum fluctuation. As a consequence, we see the continuous crossover from $N_G = 2$ to $N_G = 3$. As the potential decreases more, the plateaus mix up with the crossover and the dependence of localized electrons on the gate potential becomes linear, indicating that the crystal phase continuously transforms to the liquid phase. This continuous structural transformation is in agreement with my results in Chapter 6.

Chapter 5

CONDUCTANCE

Conductance is one of the most important properties for quantum wires, and has been intensively studies in experiments. The Luttinger liquid theory (LLT) gives the description in the high-density and low excitation energy regime, where the linearization of the Fermi surface is valid. Since deviation from the linear dispersion relation has been observed, theories beyond LLT are in need, which have not been well established due to the strong fluctuations and interactions in one-dimensional (1D) fermion systems. On the other hand, computational approaches have not yet provided concrete conductance results.

In this chapter, I study the conductance of an ideal semiconductor quantum wire, with the aid of our PIMC method based on the model described in Section 4.2, which allows the release of the linear approximation made in LLT and is able to calculate dynamic correlations in many-body systems. The conductance is obtained from the current-current correlation function according to Kubo formula,

$$G = \lim_{\omega \to 0} \frac{1}{\omega} \chi_{jj}(x, x'; i\omega)|_{x=x'=0}, \tag{5.1}$$

where χ_{jj} is the current-current correlation function defined as follows,

$$\chi_{jj}(x, x'; i\omega) = -\frac{1}{\beta\hbar^2} \langle j(x, i\omega) j(x', 0) \rangle, \tag{5.2}$$

where $\beta = 1/k_B T$. The imaginary time Fourier transform is usually defined on Matsubara frequencies $\omega_n = 2\pi n/\beta\hbar$, and,

$$j(x, i\omega_n) = \int_0^{\beta\hbar} j(x, \tau) e^{i\omega_n \tau} d\tau. \tag{5.3}$$

The fermion sign problem is handled by the fixed node approximation. A study of its effect on dynamic density-density correlation is presented in Appendix B. The density and current operators are connected by the continuum equation. The agreement between the theoretical density-density response and PIMC results support the use of fixed node approximation in my conductance study.

5.1 Spinless Noninteracting Electrons

I begin with the simplest case, i.e., the spinless noninteracting electrons. In this case, the theoretical conductance as a function of electron density can be easily worked out. According to Landauer formula Eq. 2.7, each subband of spinless electrons contributes e^2/h to the conductance. Since interactions are absent here, the subband density is given by the Fermi-Dirac distribution. So the DC conductance is given by,

$$G = \frac{e^2}{h} \sum_n \frac{1}{e^{\frac{(n+1/2)\hbar\omega_0 - \mu}{k_B T}} + 1}, \tag{5.4}$$

where μ is the chemical potential determined by the density of electrons.

In order to get the DC conductance with PIMC, I calculate the imaginary frequency current-current correlation function. In the case of one-dimensional spinless free electrons, Eq. 5.2 can be calculated analytically (Bokes and Godby, 2004), and the expression is shown in Eq. 5.5,

$$G(-i\omega) = \frac{e^2}{\hbar} \frac{1}{\sqrt{2}\pi(1 + \sqrt{1 + (-i\omega/E_F)^2})^{1/2}}, \tag{5.5}$$

which is used to extrapolate the current-current correlation function from PIMC to $\omega = 0$. A typical result is shown in Fig. 5.1.

With the same parabolic confinement while $T = 3$ K, several densities of electrons are calculated and summarized in Fig. 5.2. The data was collected

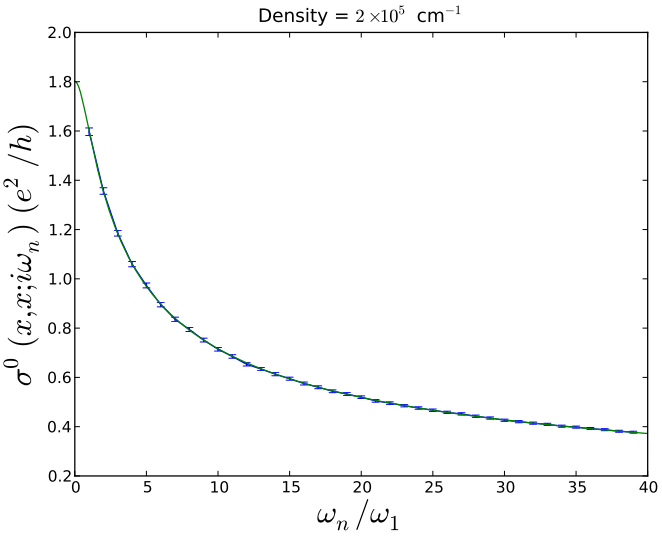

Figure 5.1: Conductance of non-interacting fermions in a parabolic wire with $\omega_1 = 5$ meV, at $T = 1.5$ K.

by my theoretical collaborator Zachary Estrada at the University of Illinois. At low densities, the two results fit well. As the density increases, the simulations take longer time to converge, furthermore, the finite size effect begins to interfere. So we see the digression from the expected curve.

5.2 Spin-Unpolarized Interacting Electrons

The Coulomb interaction, as well as the spin freedom, is added to the simulations. Two difficulties immediately emerge. First of all, the extrapolation must be carried out with caution. The exact expression for the imaginary frequency current-current correlation function of interacting electrons is still unknown. If the density of electrons are high enough so that the interaction can be treated perturbatively, it often results in shift of poles in the real frequency correlation function. For imaginary frequency, I assume that the resulting correlation function can be expressed as superposition of the noninteracting functions, so as to fit the data and extrapolate to $\omega = 0$. A result is

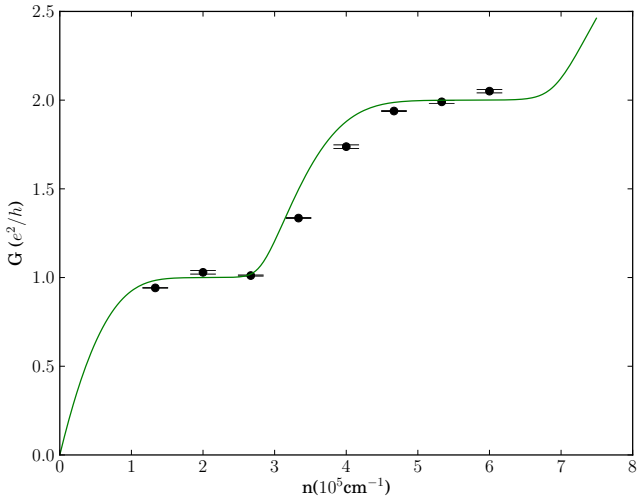

Figure 5.2: Conductance of quasi-1D spinless noninteracting electrons with $\omega_0 = 5$ meV, $T = 3$ K. The curve is the expected conductance from Eq. 5.4. This data was collected by my theoretical collaborator Zachary Estrada at the University of Illinois. While the agreement between simulation and theory are close, there are differences that are larger than the statistical error bars that require future investigation.

shown in Fig. 5.3 (the left plot). Secondly, the long range tail of the Coulomb interaction is cut off by the finite size effect, leading to uncertainty in the low frequency data.

This difficulty is aggravated at low temperature, where the sampling becomes less efficient, as is shown in Fig. 5.3 (the right plot). We cannot get the reliable DC conductance in this case. We believe that this difficulty at low temperature is actually a finite size effect. There are 48 electrons in a periodic wire of length 1.5 μm. At low temperatures, there may be quantum coherence across the supercell, leading to periodic boundary artifacts in the response. We have verified in a few cases that large simulation cells improve the density-density response, but at a much larger computational cost that quickly becomes impractical.

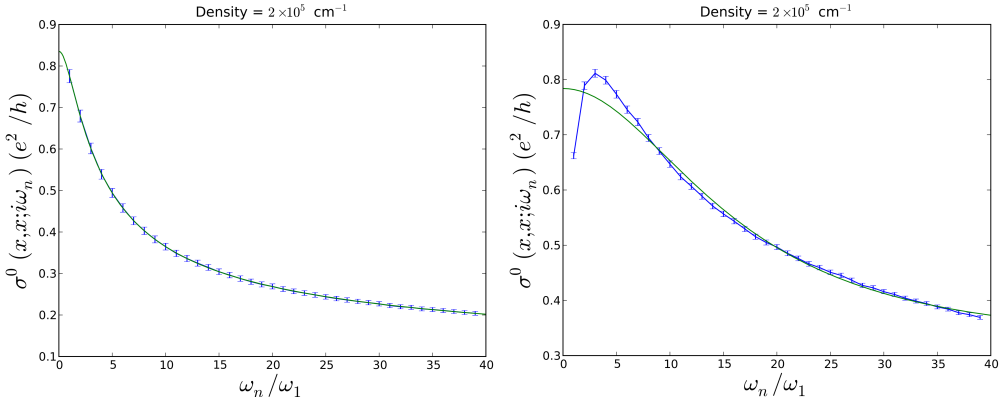

Figure 5.3: Left plot: Conductance of interacting electrons in a parabolic wire with $\omega_1 = 5$ meV at $T = 6$ K. The extrapolation to $\omega = 0$ is obtained by fitting the curve to the sum of two conductance functions for noninteracting 1D fermions. Right plot: Conductance of interacting electrons in a parabolic wire with $\omega_1 = 5$ meV at $T = 1.5$ K. The extrapolation to $\omega = 0$ is obtained by fitting the curve to the sum of two conductance functions for noninteracting 1D fermions.

Chapter 6

ZIG-ZAG ORDERING IN A QUASI-ONE-DIMENSIONAL WIRE

I study the zig-zag ordering in quantum wires with the path integral Monte Carlo (PIMC) method. For experimentally realizable electron densities, quantum fluctuations are quite large and destroy zig-zag order except at very low density, around 10^5 cm^{-1}. Zig-zag order is also sensitive to temperature, and is only visible below 1 K. The nearest-neighbor electrons tend to have antiferromagnetic spin coupling, and the next nearest-neighbor incline to ferromagnetic coupling. I estimate the spin coupling and find that it is much larger than previous theoretical estimates, which neglect quantum and thermal fluctuations of the Wigner crystal. At higher electron-density, the zig-zag structure partially transforms to a dimer state.

6.1 Introduction

It was first predicted by Wigner (Wigner, 1934) that the electrons could form crystal structure at low densities. As the density decreases, the Coulomb interaction gradually dominates over the kinetic energy, so that electrons tend to stay at the minima of the potential. To some extent, their relative positions become fixed and a crystal of electrons are formed. In three dimensions, electrons have more choices to lower their energy, so the Wigner crystal is hard to generate. Only in lower dimensions is the crystal easy to see. It is favored by the development of nanotechnology.

Interest in the quasi-1D Wigner crystal arises from the well-known "0.7 structure" in the conductance of quantum wires (Thomas *et al.*, 1996, 1998; Cronenwett *et al.*, 2002). In a strictly one-dimensional quantum wire, the quantum fluctuations are too strong to allow the existence of any crystal structure. However, when the transverse confinement is loosened, a quasi-1D wire makes Wigner crystal possible, so long as the density is sufficiently low–typically $n^{-1} < a_B$, where n is electron density and a_B is the effective Bohr radius. When the temperature T is higher than the spin coupling energy J, electrons can be considered as spinless fermions, and the wire is in the spin-incoherent regime. Theoretical works (Cheianov and Zvonarev, 2004; Fiete and Balents, 2004) have revealed quite a few interesting properties of this regime, such as the e^2/h plateau in the conductance (Matveev, 2004b,a), the phonon modes (Meyer *et al.*, 2007), as well as other aspects of transport, the zero-bias anomaly and deviation from Luttinger Liquid theory that is valid for high densities (Fiete *et al.*, 2005a,b; Matveev *et al.*, 2007; Fiete, 2007). This theory is driven by experiments. Using momentum resolved measurement of the tunneling between parallel wires, the local density of states and other properties with or without magnetic fields are obtained (Auslaender *et al.*, 2005; Steinberg *et al.*, 2006). Experiments that measure the conductance under different conditions indicate the effects of the Wigner crystal states (Crook *et al.*, 2006; Hew *et al.*, 2008; Smith *et al.*, 2009), such as the doubling of the conductance while weakening the transverse confinement (Hew *et al.*, 2009). Nevertheless, a complete picture of spin-incoherent quantum wire is not yet finished.

When $T < J$, the spin interaction needs to be taken into account based on Heisenberg model. The quasi-1D structure possesses rich features compared

to the Heisenberg chain, if the nearest-neighbor and next-nearest-neighbor coupling is considered (Klironomos *et al.*, 2007). A few methods are proposed to estimate the exchange constant J (Matveev, 2004a; Klironomos *et al.*, 2005; Fogler and Pivovarov, 2005), whereas the validity of the approximations needs further confirmation. On the other hand, due to the relatively small magnitude of J, experiments on the spin effects are still at an early stage, and the current results (Chen *et al.*, 2009) needs further study.

The structure of the Wigner crystal in quasi-1D quantum wire has been determined by numerical calculations (Piacente *et al.*, 2004). The classical Monte Carlo method reveals a zigzag pattern as the transverse confinement decreases. Further decreasing the confinement leads to multi-row configurations. The phase diagram is shown in Fig. 6.1. A quantum Monte Carlo analysis is presented in Shulenburger *et al.* (2008), where by looking at the static dynamic structure factor, they observed peaks at $4k_F$ under certain combination of the electron density and the transverse confinement, which is the feature of a quasi-Wigner crystal in quasi-1D quantum wires. Their results partially explained the experiments (Steinberg *et al.*, 2006).

In this paper, I perform quantum Monte Carlo calculations based on path integral at finite temperature. My simulation conditions are also shown in Fig. 6.1. I calculate the pair correlation function to study properties of the zigzag state, and estimate the magnitude of the spin coupling. I also find the dimer state and the corresponding exchange energy.

6.2 Method

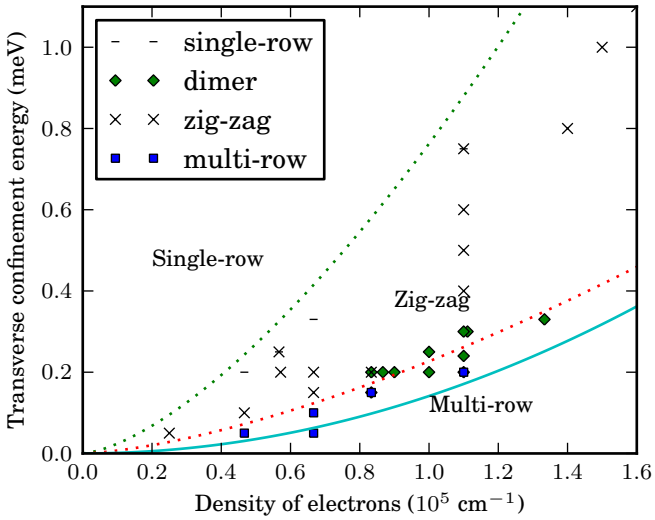

Figure 6.1: The phase diagram from classical simulations of Piacente *et al.* (2004) (the continuous lines) and my simulations around $T = 0.2$ K (data points).

The study in this chapter is based on the quasi-one dimensional model described in Section 4.2.

6.2.1 Classical Monte Carlo

Before simulating the quantum mechanical system, I perform classical simulations, which are applicable at low electron density. These classical systems serve as a control system to assess the effects of quantum fluctuations.

In the classical simulation, I put 40 distinguishable charged particles in a 6000 nm wire. I do not have the image particles included, since the long range tail of the Coulomb interaction does not make a difference here.

In order to compare to the quantum simulation, I put 20 spin-up electrons and 20 spin-down electrons in the same wire, while leaving the other conditions unchanged. I have to maintain the low temperature, since the density is so low that a low temperature is necessary in order not to overcome the Fermi energy. I put the image electrons 500 nm below the wire.

6.2.2 Path Integral Monte Carlo

With PIMC, we don't need to design a trial function as in other quantum Monte Carlo methods, just to run simulations longer to obtain the desired error. And we can easily obtain the thermal dynamic properties at nonzero temperatures.

To deal with the minus sign problem inherent in fermion simulations, we apply the fixed-node approximation (Reynolds *et al.*, 1982). At 1D, this approximation is exact. For quasi-1D wires, we use Eq. 3.12 to define the nodes.

To avoid any artificial bias, I initially put all electrons along the center of the wire. When the zig-zag is present, it is highly possible that the electrons are locked into a special configuration, which causes ergodicity problem. Therefore, I sample the swap moves between electrons of different spins. I also sample the collective moves of electrons along the longitudinal direction of the wire, in order to preserve the translational symmetry. The density is controlled by the length of the wire, and the width of the wire is determined by ω in $V(\mathbf{r})$. Periodical boundary condition is applied.

6.2.3 Zig-zag order parameter

The pair correlation function is plotted. To quantify the correlation between particles, I define a parameter ξ as in Eq. 6.1,

$$\xi(\Delta x) = -\frac{2\langle y_1(\Delta x) y_2\rangle}{\langle y_1^2\rangle + \langle y_2^2\rangle}. \tag{6.1}$$

where y_1 and y_2 are the relative y-direction distance from the two particles to the center of the wire respectively. With two particles, ξ has a clear meaning: $\xi = 0$ when no zig-zag and $\xi = 1$ when zig-zag is present. For many particles, ξ displays the correlation with respect to the relative spacing between particles.

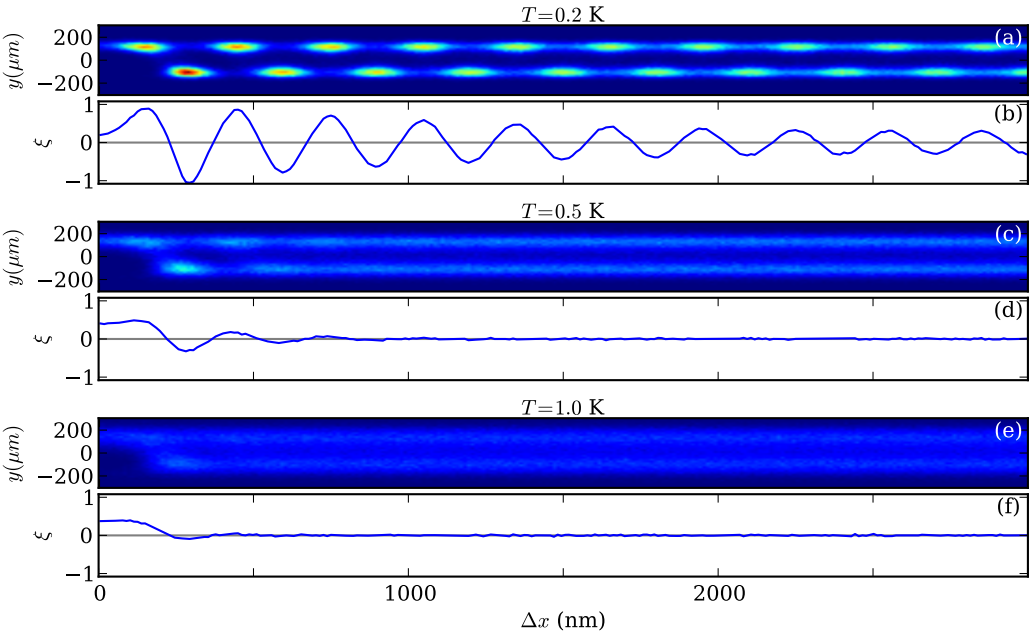

Figure 6.2: Pair correlation function of a classical simulation of a 6-micron wire with 40 charged particles. The parabolic confinement is 0.2 meV. The reference particle is placed at the center of the second row.

In my simulations, I collect pair correlation function $g(y_1, y_2, \Delta x)$ for evaluating the numerator of Eq. 6.1, and density ρ for evaluating the denominator of Eq. 6.1,

$$\xi(\Delta x) = -\frac{2\int y_1 y_2 g(y_1, y_2, \Delta x) dy_1 dy_2}{\int y_1^2 \rho(y_1) dy_1 + \int y_2^2 \rho(y_2) dy_2}. \tag{6.2}$$

My results are shown in Fig. 6.2.

6.3 Results

6.3.1 The classical system

My results are not in perfect agreement with Piacente *et al.* (2004). Under the same conditions, their results are in the regime of multi-row Wigner crystal. The discrepancy is probably due to the different treatment of the Coulomb interaction. For this classical simulation, I calculate the Coulomb interaction

directly without any approximation. Thanks to the simplicity of classical systems, it does not cost too much CPU time.

At the density I select, the Coulomb interaction dominates over the confinement. Competition between the two potentials gives rise to local minima in the pattern of zig-zag. Fig. 6.2 illustrates how the zig-zag melts down as the temperature increases. At low temperature, the classical wire displays long range ordering. The correlation decays exponentially. The tails are suppressed at high temperature by thermal fluctuation. At 1 K, the ordering in a single row is destroyed, but we can still see two rows since the thermal energy is still below the first subband.

6.3.2 Suppression of zig-zag by quantum fluctuations

I then add the quantum effects into the system. The resulting pair correlation functions are shown in Fig. 6.3. The pair correlation function still displays a true Wigner crystal, especially in the total correlation plot, whereas the correlation washes out beyond the sixth nearest electrons. It indicates the strong effects of quantum fluctuation. As the density increases, the quantum fluctuations increase so fast that they smear out the crystal structure at a density around 10 electrons per micron, which is still lower than the densities in experiments (Steinberg *et al.*, 2006; Hew *et al.*, 2009). On the other hand, reducing the transverse confinement gradually widens the two rows and finally leads to three-row Wigner crystal, which is consistent with classical results (Piacente *et al.*, 2004). The thermal fluctuation behaves the same as in the classical simulations, the difference is that the zigzag melts earlier with the presence of the quantum fluctuation, at around $T = 0.5$ K.

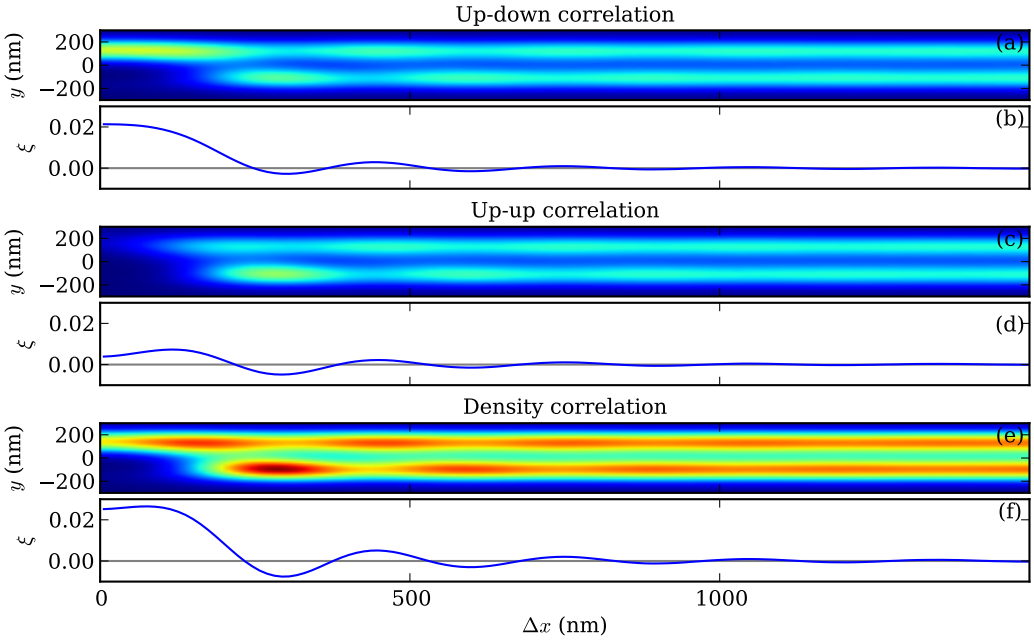

Figure 6.3: Pair correlation function of a quantum simulation of a 6-micron wire with 20 spin-up electrons and 20 spin-down electrons. The temperature is 0.2 K and the parabolic confinement is 0.2 meV. The reference spin-up electron is placed at the center of the second row.

6.3.3 Enhancement of spin coupling

In strict 1D quantum wire, spontaneous spin polarization is forbidden according to the Lieb-Mattis theorem (Lieb and Mattis, 1962)d Howevek, in quasi-1D, it is possible to see spin ordering under certain conditions. Fig. 6.3 also indicates the discrepancy between electrons of different spins. Electrons of opposite spins tend to stay in the other row, while electrons of the same spins stay in the same row. That provides a possible way of looking at the spin interaction. Since I have a true Wigner crystal, I take the data from Fig. 6.3 and discretize the pair correlation function by separating the area of each electron from others, then calculate the pair correlation function in each area, as shown in Fig. 6.4 and Fig. 6.5.

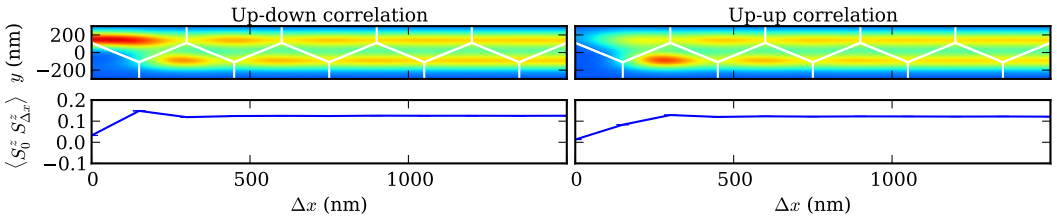

Figure 6.4: Discretization of the continuum pair correlation function and the correlation between lattice sites. The left-right symmetry has been used to reduce the error bar.

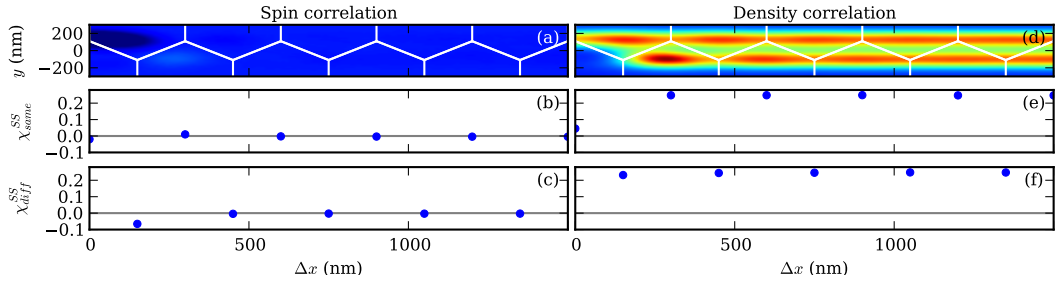

Figure 6.5: Discretization of the continuum pair correlation function and the correlation between lattice sites. The left-right symmetry has been used to reduce the error bar.

Now I have a lattice model, on each site of which there is only one electron with a certain spin state. The pair correlation function can now be considered as correlation between spins on different sites. Thus the up-down correlation function shows antiferromagnetic coupling and the up-up correlation shows ferromagnetic coupling. By subtracting the up-down correlation from the up-up correlation, we get the net spin coupling in the zig-zag structure. Note that at $\Delta x = 0$, the spin correlation is not 0. This is because the fluctuations smear out the perfect crystal structure and the discretization introduces some systematic error. It is clear that the nearest-neighbor coupling is antiferromagnetic, and the next-nearest-neighbor coupling is ferromagnetic. Frustration causes the ferromagnetic correlation on the next-nearest-neighbor decays faster. From Fig. 6.4, I have the data as in Table. 6.1.

Since in my PIMC calculations, the rotational symmetry of spins is preserved, the spin coupling is described by the Heisenberg model. I use a lattice

Table 6.1: Spin correlation and the corresponding coupling constants.

ordering	$\langle S_0 S_1 \rangle$	$\langle S_0 S_2 \rangle$	J_0 (meV)	J_1 (meV)
zigzag	-0.279(9)	0.051(9)	0.018(3)	0.0008(7)
dimer	-0.236(7)	0.048(7)	0.014(3)	-0.0036(9)

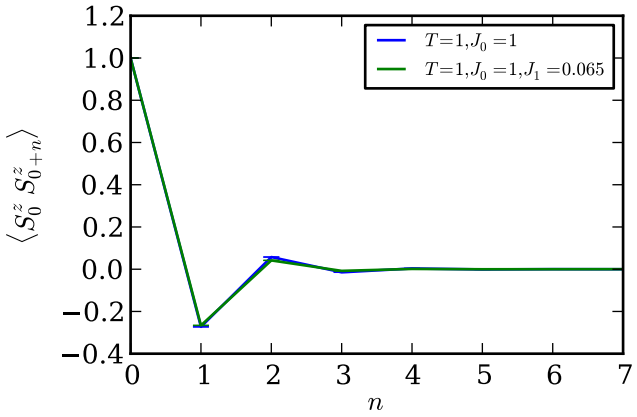

Figure 6.6: Spin correlations with different coupling constants. It is clear that the zigzag is frustrated, otherwise the correlation between the next-nearest-neighbor spins are greater than my PIMC results.

quantum Monte Carlo method from the ALPS package (ALP, 2011; Alet *et al.*, 2005b,a; Troyer *et al.*, 1998) to explicitly simulate the spin interaction in my model. I tune the coupling constant J_0 for the nearest neighbor and J_1 for the next nearest neighbor and run the lattice quantum Monte Carlo simulation until it gives the same correlations as in my PIMC results. The results are shown in Fig. 6.6. By comparing the spin correlation, I am able to determine the exchange energies Table. 6.1, where the error is calculated by error propagation Eq. 6.3. Since $J_1 > 0.24 J_0$, my results are in agreement with theoretical phase diagram (Klironomos *et al.*, 2007).

$$\Delta J_0 = \sqrt{\left(\frac{\partial J_0}{\partial \chi_0}\right)(d\chi_0)^2 + \left(\frac{\partial J_0}{\partial \chi_1}\right)(d\chi_1)^2}, \qquad (6.3)$$
$$\chi_0 = \langle S_0 S_1 \rangle, \quad \chi_1 = \langle S_0 S_2 \rangle.$$

We see that the nearest-neighbor exchange energy is much greater than the prediction in Matveev (2004a). It should be noted that Matveev (2004a) calculates the exchange coupling by assuming the exchange of only two electrons, and does not take into account of the change in the potential due to correlations of other electrons to the exchanging particles, as well as other many-body effects. Theoretically it is not easy to evaluate how good their estimation is. My result suggests that in the zig-zag state, the exchange energy between antiferromagnetic electrons is enhanced. It makes sense, considering the spin coupling can be regarded as localized Coulomb interaction and the zig-zag is in the strong-interaction regime.

6.3.4 Dimer states

For spin-unpolarized electrons, the formation of zigzag requires a very low density. As the density and the confinement potential increases, the Coulomb interaction gradually loses the dominant position, giving way to other interactions. Due to Pauli's exclusion, there is still strong repulsion between electrons of the same spin. But a spin-up electron and a spin-down electron could bind together and form a dimer state, as shown in Fig. 6.7.

Unlike the Cooper pair, which is mediated by electron-phonon interaction, the dimer state is the result of spin coupling when the Coulomb interaction is still strong. It is a singlet across the double-row configuration. Thus, I use the same discretization method as in the analysis of the zigzag spin coupling. The results are shown in Fig. 6.8.

We can see that the antiferromagnetic coupling, as well as the ferromagnetic coupling, in the dimer state is nearly as strong as the ones in zigzag. The

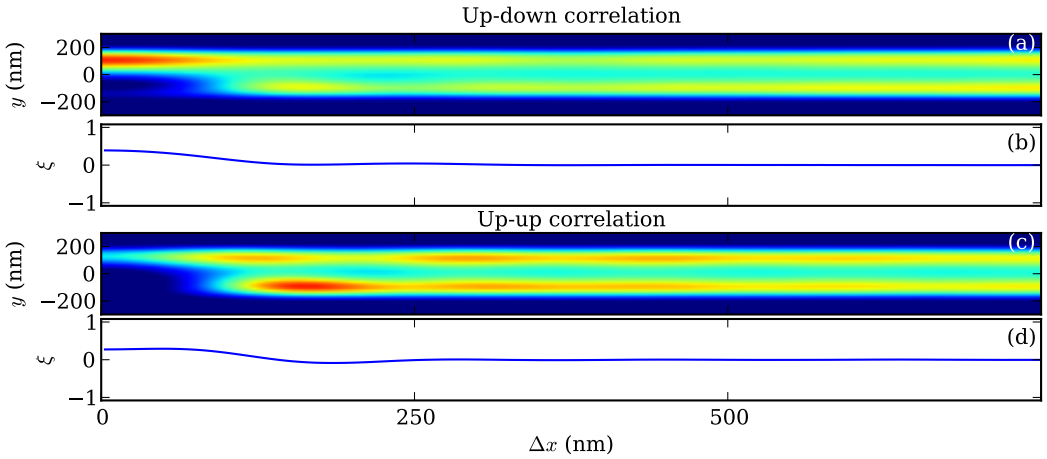

Figure 6.7: Pair correlation function for dimer state at 0.2 K. The reference electron is in the center of the lower row. The density is halved with respect to Fig. 6.3. The confinement energy is 0.33 meV. For spin-polarized electrons, the same conditions lead to zigzag.

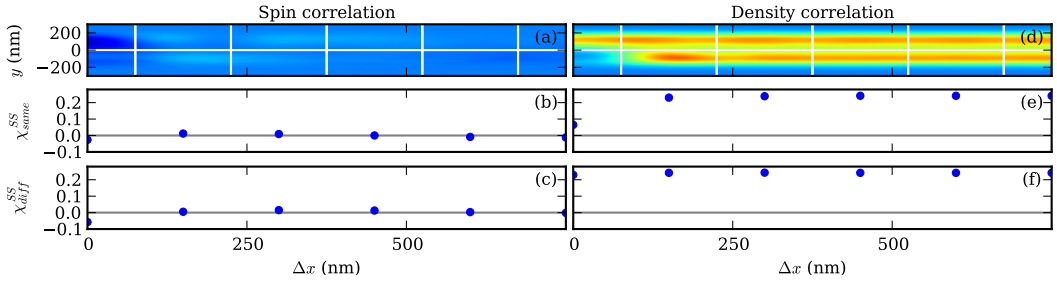

Figure 6.8: Discretization of the dimer state. In the 2nd and the 4th plot, the x coordinate is the distance from each lattice site to the reference site which is around (0,-150).

difference is that the nearest neighbor is in the same row, and the next-nearest neighbor is in the other row. It is understandable, since the spin interaction decays fast as two electrons separate, and the low density makes the separation far enough to be insensitive to the transition from zigzag to dimer. On the other hand, the increasing density weakens the Coulomb interaction with respect to the kinetic energy, so that the little preference in the spin pairing makes a difference. It should be noted that the spin interaction only changes the ordering in the same row a little, it is not a prominent effect. A spin Monte Carlo calculation based on ladder structure gives the spin coupling for the above correlation Table. 6.1. We can see that $J_0 > -0.24J_1$, consistent with Klironomos *et al.* (2007). My result is near the critical point between the dimer state and the antiferromagnetic state. This estimation of the coupling constants is coarse, since the dimer state in my results is a short-range effect and the interaction between dimers is very weak, not exactly comparable to a rigid ladder structure in the spin Monte Carlo simulation. So one needs to be careful how to deal with the interaction in the same row. Nevertheless, it displays significant differences from the spin coupling in zigzag, where there is only antiferromagnetic coupling.

Chapter 7

QUANTUM POINT CONTACT

A quantum point contact (QPC) is a widely used implementation for quantum dots and quantum wires. It allows fine tuning of the electron density and the transverse confinement, and the conductance measurement under different conditions. Experiments on QPCs have revealed many interesting features of quantum wires, such as the properties of the spin-incoherent Luttinger liquid (Thornton *et al.*, 1986; Hew *et al.*, 2008), the "0.7 structure" in conductance and its relation to the width of the wire (Smith *et al.*, 2009; Hew *et al.*, 2009), the external magnetic field (Thomas *et al.*, 1998) or the temperature (Kristensen *et al.*, 1998, 2000; Cronenwett *et al.*, 2002), the spin polarization and g factor (Patel *et al.*, 1991; Thomas *et al.*, 1996; T.-M.Chen, 2008). The observed jumps of conductance at low density, low confinement regime provides an indirect evidence of the existence of the zig-zag state (Hew *et al.*, 2009). With the knowledge obtained in the Chapter 6, I model the QPC with the Timp potential (Timp, 1992), and study the electron states in this specific configuration.

7.1 The Model

The Timp potential is defined as follows

$$\begin{aligned} V(x,y) =& f\left(\frac{2x-L}{2Z}, \frac{2y+W}{2Z}\right) - f\left(\frac{2x+L}{2Z}, \frac{2y+W}{2Z}\right) \\ &+ f\left(\frac{2x-L}{2Z}, \frac{-2y+W}{2Z}\right) - f\left(\frac{2x+L}{2Z}, \frac{-2y+W}{2Z}\right), \end{aligned} \tag{7.1}$$

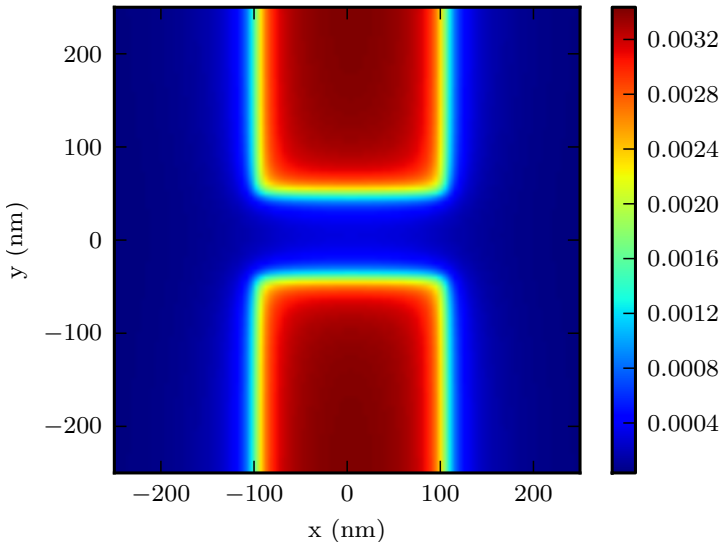

Figure 7.1: A typical Timp potential for our simulations on QPC. The channel is 90 nm wide, 200 nm long. The two split gates are $z = 10$ nm above the 2D electron gas, with a voltage of -0.1 V. The color bar shows the magnitude of the potential in Hartrees.

where L is the length of the channel between the split gates, W is the width of the channel, Z is the height of the gates above the two-dimensional electron gas, and function f is defined as follows

$$f(u,v) = -\frac{V_G}{2\pi\left(\frac{\pi}{2} - \arctan(u) - \arctan(v) + \arctan(\frac{uv}{\sqrt{1+u^2+v^2}})\right)}, \qquad (7.2)$$

where V_G is the gate voltage. It approximates the solution to the electrostatic problem with two metallic split gates in a medium. Its shape is shown in Fig. 7.1. In our simulations, we keep the height of the gates fixed at $z = 10$ nm above the 2D electron gas, and tune the width and the voltage to control the potential between the gates. With a negative voltage, the gates deplete electrons below them, so that the channel between them can be considered as a quantum wire. Compared to the parabolic confinement we use in the study of zig-zag, this model is a better representation of the process in experiments.

7.2 Localization of Electrons with Increasing Confinement

I use 500×500 nm supercell, 30 electrons in total and 5 K as the temperature. As the voltage of the split gates increases, electrons are squeezed out of the channel. The decrease of the electron density inside the channel leads to strong Coulomb interaction. The localization of electrons in the center of the channel is formed, which is consistent with the results in the literature (Güçlü *et al.*, 2009). The high electron density at the entrances of the channel indicates Coulomb blockade. Fig. 7.2 shows the process of the formation.

In order to compared with my results for the zig-zag state in last chapter, I estimate the equivalent parabolic confinement for each gate voltage. I take the transverse density profile at the center of the channel, assume that it is the ground state density of a one-dimensional simple harmonic oscillator, calculate the spread of the density $\langle y^2 \rangle$, which should then be equal to the quantum width of a simple harmonic oscillator $\sqrt{\hbar/m\omega_0}$. The resulting ω_0 is shown on each density plot.

With the presence of localization, the conductance of the QPC is reduced to e^2/h theoretically. I calculate the imaginary current-current correlation function, and use Kubo formula to obtain the DC conductance at the center of the channel. As is shown in Chapter 5, when extrapolating the correlation function to $\omega \to 0$, I use the linear combination of the correlation functions for one-dimensional noninteracting electron gas Eq. 5.5. It turns out that a sum of two of the noninteracting functions is able to give nice fit. Fig. 7.3 shows the conductance for Fig. 7.2(c). Fig. 7.4 shows the one-dimensional electron density inside the channel and the conductance as a function of gate voltage. As the voltage on the gates increases, the linear density decreases. In the

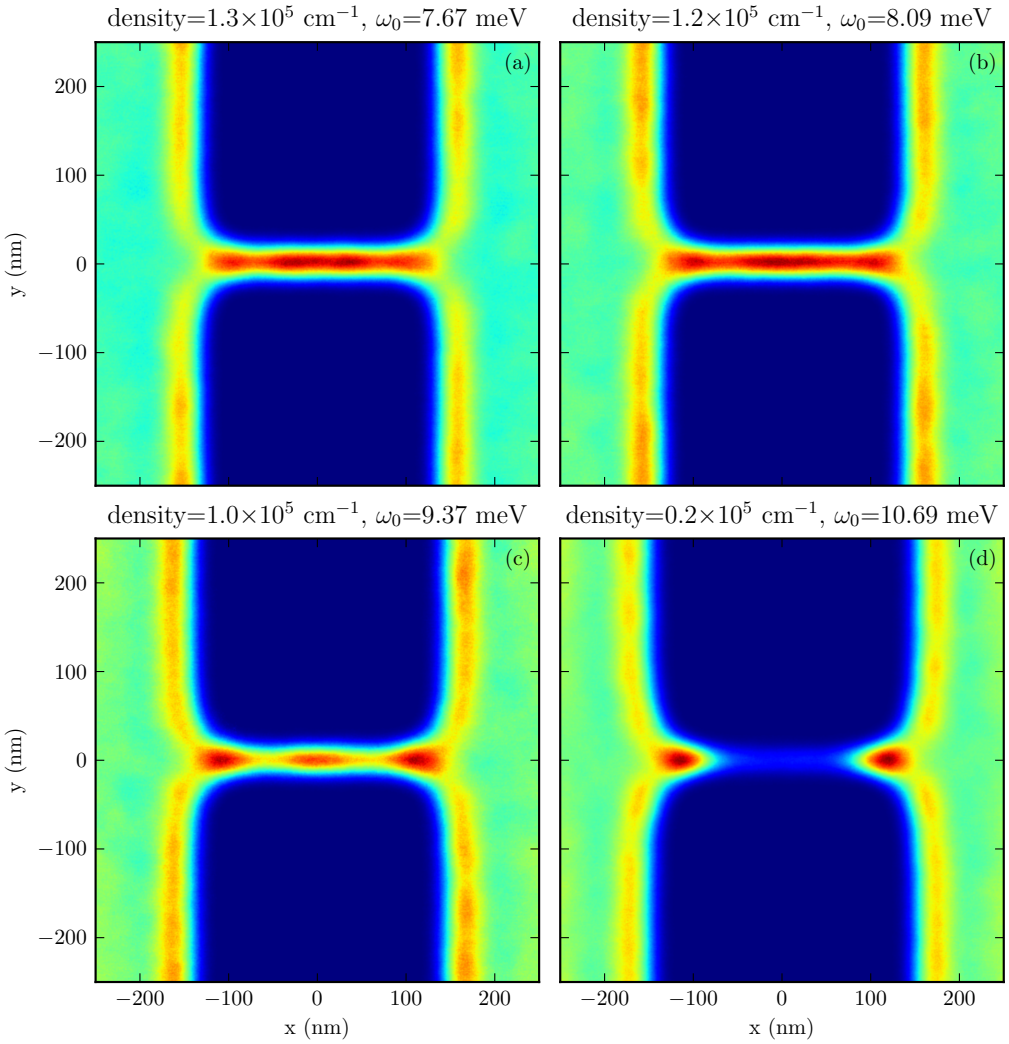

Figure 7.2: Density of electrons. 500 × 500 nm supercell, 30 electrons, T = 5 K. For the QPC: width = 90 nm, length = 200 nm, height of split gates = 10 nm. Gate voltage for each plot is (a) -0.07 V; (b) -0.08 V; (c) -0.11 V; (d) -0.16 V. The one-dimensional electron densities inside the channel and the estimated parabolic confinements are show on top of each graph.

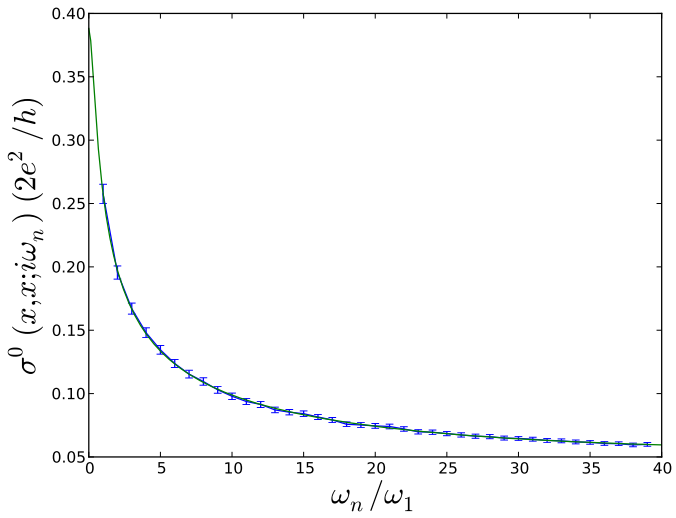

Figure 7.3: Current-current correlation function for Fig. 7.2(c) and the extrapolation to $\omega \to 0$. The fitting curve is the sum of two correlation functions for noninteracting electron gas.

middle range where the single localization takes place, the decrease is a little slower, indicating the effect of Coulomb interaction. In this regime, a plateau at $0.4(2e^2/h)$ is formed. The deviation from $0.5(2e^2/h)$ implies the effect of interaction on conductance.

7.3 The Possible Zig-Zag State

Based on my study for the zig-zag state in a parabolic confinement, I lower the electron density in the channel while tuning the separation between the split gates to search for the zig-zag state in QPC. The difficulty here is that one cannot control the density in the channel directly, which results from the density of the two-dimensional electron gas outside the gates, the voltage of the gates and the separation between the gates. I keep the voltage fixed at -0.1 V and the number of electrons at 30. By enlarging the supercell, I can lower the density of the whole system. For each size of supercell, I run a series of simulations with different separation between the gates. The temperature is

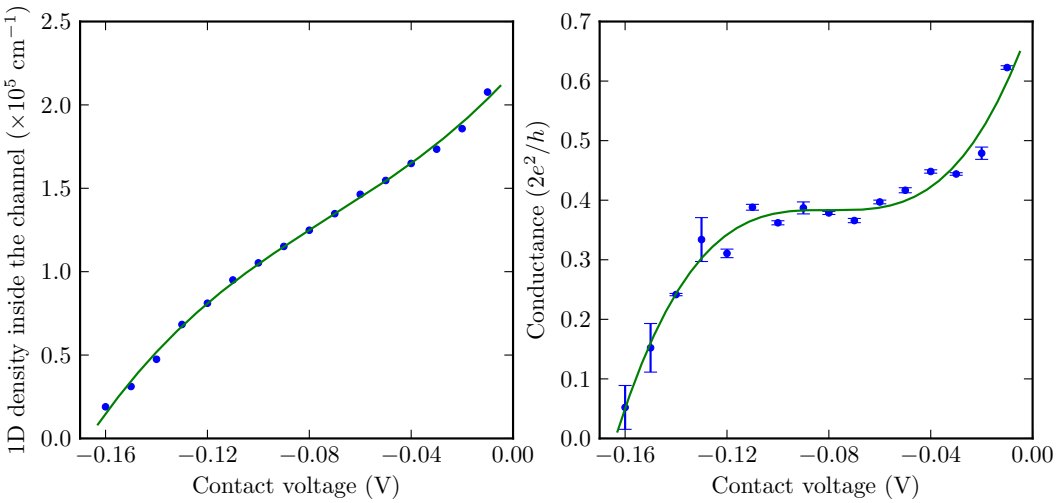

Figure 7.4: The one-dimensional density inside the channel and the DC conductance as a function of the gate voltage. For localization states, the conductance is around $0.4(2e^2/h)$. As the voltage decreases, the electrons in the channel become more and more as free electrons, so the conductance increases.

first set to 5 K, so that the simulations converge fast. Once the desired density and confinement is reached, the temperature is then set to 1 K to begin a new simulation with less thermal fluctuation, to which the zig-zag is sensitive.

I first note that when the separation is set to 180 nm, two rows of electrons are formed in the channel at 5 K, as is shown in Fig. 7.5. The conductance is shown in Fig. 7.6.

I then set the temperature to 1 K. Due to the increasing imaginary-time length of paths, the simulation converges slowly. The density is shown in Fig. 7.7. To identify the zig-zag state, I look at the pair correlation function. Fig. 7.8 shows the probability distribution of spin-down electrons when a reference spin-up electron is placed at the white crossing. A pattern of zig-zag can be identified, although it is not a strong feature. It should be noted that at $1K$ in the parabolic confinement, zig-zag state is destroyed by the fluctuations. So the electron crystal is actually enhanced a little in quantum point contact.

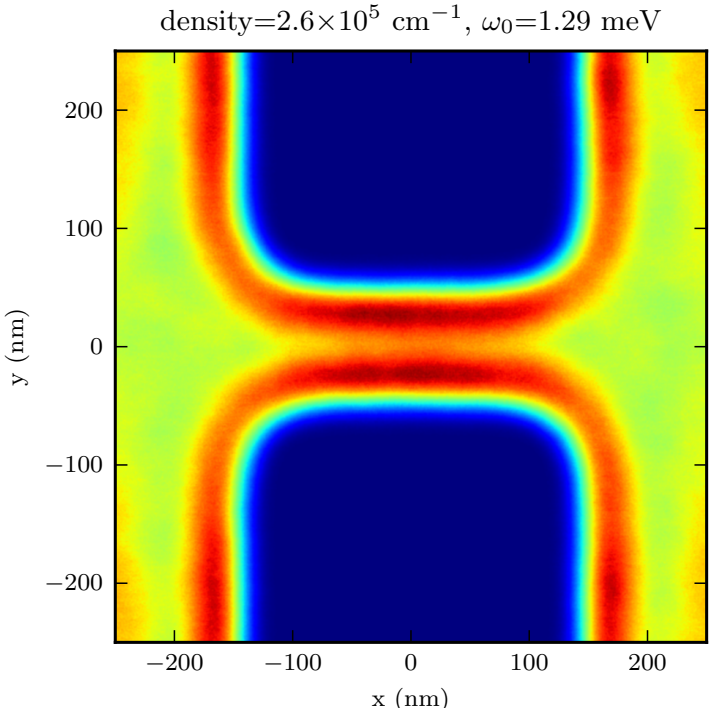

Figure 7.5: Electron density for 500 × 500 nm supercell and 30 electrons at 5 K. The two-row structure with the density and confinement suggests a possible zig-zag state at lower temperature.

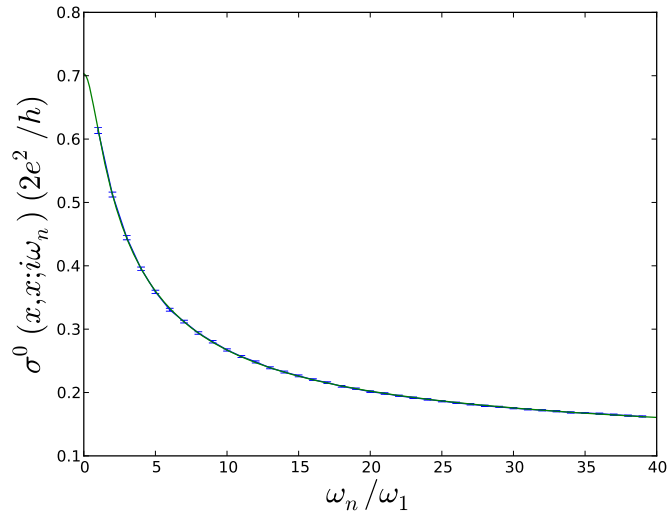

Figure 7.6: Current-current correlation function for Fig. 7.5.

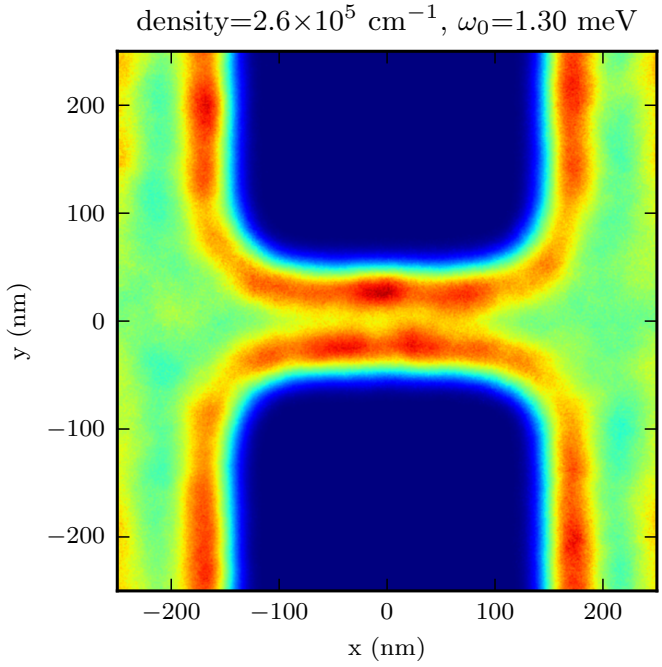

Figure 7.7: Electron density for 500 × 500 nm supercell and 30 electrons at 1 K.

This feature is supported by the latest study on the surface electron state on liquid helium (Rees *et al.*, 2012) The conductance is shown in Fig. 7.9. It is interesting to note that this conductance is very near $0.7(2e^2/h)$.

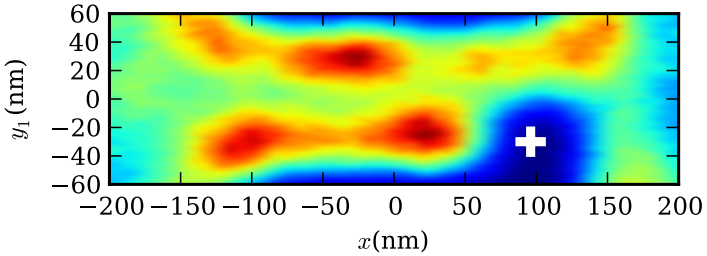

Figure 7.8: The pair correlation function for Fig. 7.7. A reference spin-up electron is placed at the white crossing, and the plot is the probability distribution of finding a spin-down electrons with respect to the reference electron. Although it is not a strong signal, we can still see the pattern of zig-zag.

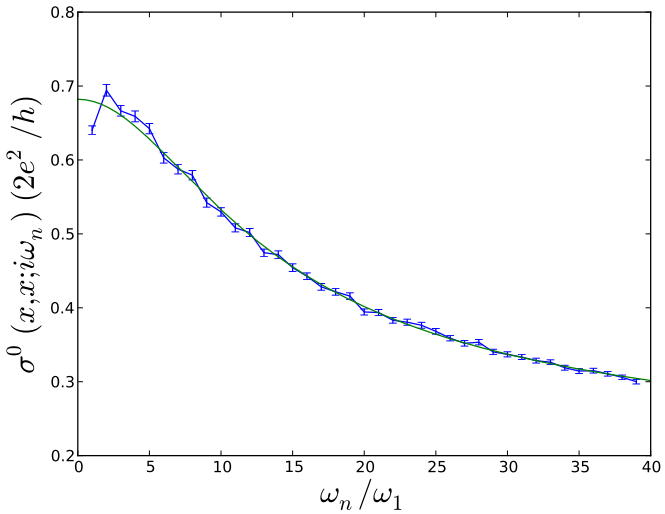

Figure 7.9: Current-current correlation function for Fig. 7.7, for a zig-zag state in a quantum point contact. The extrapolation to the DC limit, $\omega_n \to 0$, gives a conductance very near $0.7(2e^2/h)$.

Chapter 8

CONCLUSION

In this dissertation, I study the physics of quantum wires by means of the path integral Monte Carlo (PIMC) method. PIMC allows me to calculate the finite temperature responses of electron systems under specified conditions.

I first study the general properties of quantum wires that can be interpreted by the Luttinger liquid theory. I calculate the imaginary time current-current correlation function. By extrapolating it to the zero response frequency $\omega = 0$, I obtain the conductance according to the Kubo formula. The conductance of a one-dimensional (1D) electron gas fits well with the theoretical prediction.

Secondly, I study the low electron density regime for quasi-1D quantum wires. Since the Coulomb interaction dominates over the quantum fluctuations in this regime, it is believed that an electron state called Wigner crystal is formed in wires. Although in 1D, an electron crystal is impossible due to the strong quantum fluctuations, in quasi-1D, my results show the existence of a zig-zag structure, as is predicted by classical simulations. The quantum fluctuations make the the zig-zag only a local effect. I define an order parameter $\xi(x)$ in order to quantitatively describe the transition from a single line to a zig-zag. A look into the correlation between electrons of different spins shows that the nearest spin correlation is anti-ferromagnetic, and the next-nearest correlation is ferromagnetic. The correlation provides a way to estimate the spin coupling strength, which turns out to be much less than the pencil-and-paper estimation. It should be noted that the pencil-and-paper estimation does not take the many-body effect into account, and thus is a

rough approximation. By tuning the transverse confinement and the electron density, I find a dimer state in which electrons of opposite spins are coupled across the double rows of zig-zag. I plot a phase diagram to summarize the results.

Finally, I study the quantum point contact by building up a model of the same configuration using a Timp potential. I first find that as the split gate voltage increases, the narrowing of the channel culminates in localization of single electrons in the middle of the channel at 5 K. This localized electron causes Coulomb blockade, which is consistent with the results in the literature. I calculate the conductance of this state with the method from Chapter 5. A clear plateau around $0.4(2e^2/h)$ is shown, indicating the effect of the Coulomb interaction. I then try to search for the possible zig-zag state in quantum point contact. In order to use the results from Chapter 6, I estimate the equivalent parabolic confinement from the density profile. In the regime of zigzag according to the phase diagram from Chapter 6, I find the pattern of Wigner crystal at 1 K. The temperature here is higher than it is for the parabolic confinement, indicating the enhancement of the robustness. The estimated conductance of this zig-zag state is very close to $0.7(2e^2/h)$.

APPENDIX A

COULOMB ACTION

The Coulomb action is considered as

$$S_C = -\log(\rho) - S_{free} \tag{A.1}$$

where S_{free} is the free particle action, ρ is the density matrix satisfying the Bloch equation

$$-\frac{\partial}{\partial\tau}\rho = \left(-\frac{\nabla^2}{2m_{ij}} + \frac{q_i q_j}{r_{ij}}\right)\rho \tag{A.2}$$

where m_{ij} is the reduced mass of particle i and j. Here we only consider S_C as a pair action, ignoring the higher order terms. We assume that the Coulomb action takes the form

$$S_C = \sum_{i,j} u(|\mathbf{r_i} - \mathbf{r_j}|, \Delta\tau) \tag{A.3}$$

where

$$u(r, \Delta\tau) = \frac{a_0 + a_1 r + a_2 r^2}{1 + b_1 r + b_2 r^2 + b_3 r^3} \tag{A.4}$$

The coefficients a_i and b_i are determined by fitting the action to numerical solutions of Eq. A.2 as well as the known values at $r \to 0$ (Pollock, 1988) and $r \to \infty$ (Vieillefosse, 1994a,b).

In experiments, the top gates can be mimicked by image charges in simulations. So the Coulomb action we use becomes

$$S_C = \sum_{i,j} \left[u(|\mathbf{r_i} - \mathbf{r_j}|, \Delta\tau) - u(\sqrt{|\mathbf{r_i} - \mathbf{r_j}|^2 + d^2}, \Delta\tau)\right], \tag{A.5}$$

where d is the distance from the image charges to the 2D electron gas. The image charges also cut off the long range tail of the Coulomb interaction.

APPENDIX B

DENSITY-DENSITY RESPONSE OF NON-INTERACTING ELECTRONS

The retarded density-density response function for a homogeneous system is defined as

$$\chi_{nn}(\vec{x},t) \equiv -\frac{i}{\hbar}\Theta(t)\langle[\hat{n}(\vec{x},t),\hat{n}(0)]\rangle \tag{B.1}$$

where the $\langle\rangle$ means thermal average, and $\Theta(t)$ is the step function. It is usually studied in the momentum and frequency domain:

$$\chi_{nn}(\vec{q},\omega) \equiv \frac{1}{L^d}\int d^d r \chi_{nn}(\vec{x},t)e^{-i\vec{q}\cdot\vec{x}+i\omega t} \tag{B.2}$$

where d is the dimension.

For non-interacting electrons, χ_{nn} can be calculated analytically, and the expression is (Giuliani and Vignale, 2005)

$$\chi_{nn}(\vec{q},\omega) = \frac{1}{L^d}\sum_{\vec{k},\sigma}\frac{n_{\vec{k},\sigma}-n_{\vec{k}+\vec{q},\sigma}}{\hbar\omega+\epsilon_{\vec{k},\sigma}-\epsilon_{\vec{k}+\vec{q},\sigma}+i\hbar\eta} \tag{B.3}$$

where $n_{\vec{k},\sigma}$ is the Fermi-Dirac distribution, $\epsilon_{\vec{k},\sigma}$ is the energy of a single electron, η is an infinitesimal. At finite temperature, usually one cannot work out the summation in Eq. (B.3). However, it can be evaluated easily with numerical method for imaginary frequency ($\omega \to i\omega$), thus can be compared with our PIMC results directly.

In PIMC, the simulation of fermionic system is achieved by the fixed node method. In 1D, it is exact. So it is expected to show the same density-density response as B.3. In higher dimensions, we can obtain a sense of how good the approximation is, as far as the density-density response is concerned.

I plot $\chi_{nn}/N(0)$ vs. q_x/k_F for the first Matsubara frequency $\omega = 2\pi/\beta\hbar$ and $q_y = q_z = 2\pi/L$, where $N(0)$ is the density of states per volume at the Fermi energy(Giuliani and Vignale, 2005),

$$N(0) = \begin{cases} \frac{mk_F}{2\pi^2\hbar^2}, & 3D \\ \frac{m}{2\pi\hbar^2}, & 2D \\ \frac{m}{\pi\hbar^2 k_F}. & 1D \end{cases} \tag{B.4}$$

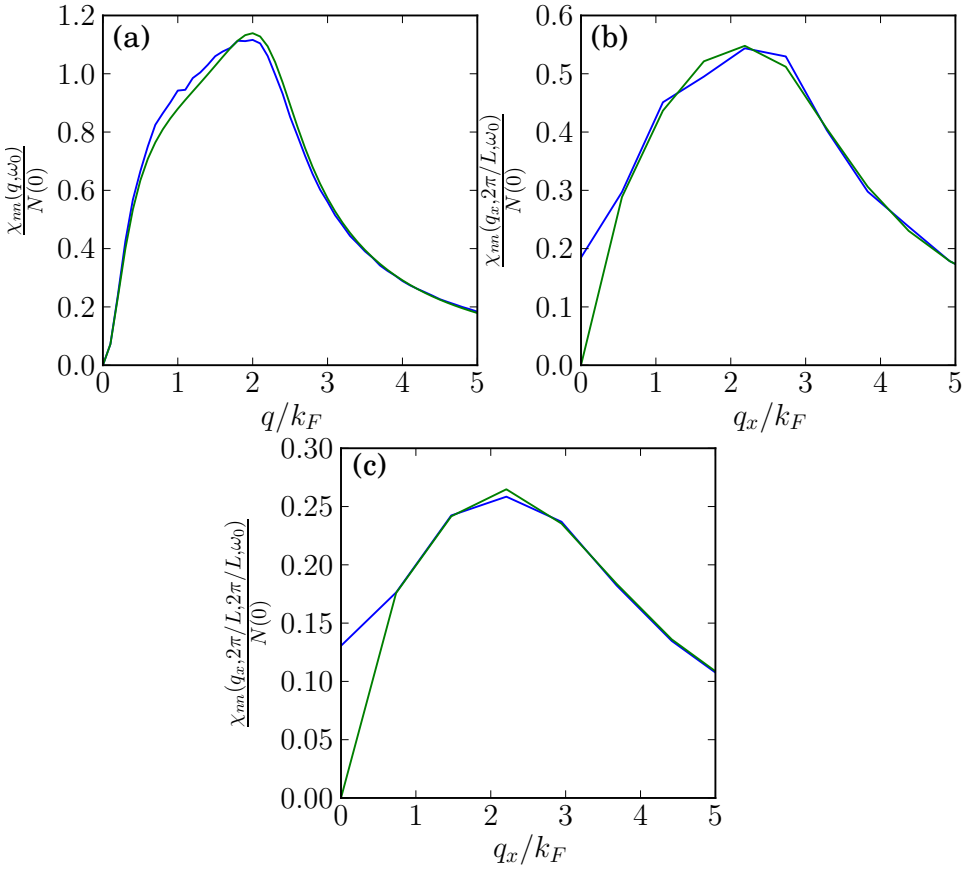

Figure B.1: The density-density response for (a) 1D with $T = 2$ K and $L = 320$ nm; (b) 2D with $T = 0.5$ K and $L = 200$ nm; (c) 3D with $T = 0.5$ K and $L = 200$ nm. Because of the finite size effect in both the theoretical evaluation and the PIMC simulation, the long wavelength response is cut off, so that $\chi_{nn}(\vec{q} = 0) = 0$. For the 2D and 3D results, the nonzero behavior at $q = 0$ in PIMC result is because of the nonzero q_y and q_z.

The results are summarized in Fig. B.1. In every dimension, the two results show good fit. The fixed node approximation does not have much effect in evaluating the density-density correlation. This is also a good support to my results on correlation functions.

APPENDIX C

PARALLELISM

The PIMC algorithm can easily take advantage of parallel computing. We clone the model on each CPU core involved. That is, we initiate the same simulation on each CPU core, but the random number seed is different, so that the simulations come out differently. Each clone then runs independently, until the measurements are collected. Thus by using clones, we increase the number of samplings and measurements per unit time, so that the simulations converge faster. We use the Message Passing Interface (MPI) to collect the results between clones.

My simulations run on Saguaro, the cluster of the Arizona Advanced Computing Center (A2C2). The typical number of clones is 16. Since error is dependent on $\frac{1}{\sqrt{N-1}}$, where N is the number of measurements, 16 clones reduce the error bar by about a factor of 4.

"Alps project", URL `http://alps.comp-phys.org/` (2011).

Alet, F., P. Dayal, A. Grzesik, A. Honecker, M. Körner, A. Läuchli, S. R. Manmana, I. P. McCulloch, F. Michel, R. M. Noack, G. Schmid, U. Schollwöck, F. Stöckli, S. Todo, S. Trebst, M. Troyer, P. Werner and S. Wessel, "The alps project: Open source software for strongly correlated systems", J. Phys. Soc. Jpn **74**, 30 (2005a).

Alet, F., S. Wessel and M. Troyer, "Generalized directed loop method for quantum monte carlo simulations", Phys. Rev. E **71**, 036706 (2005b).

Auslaender, O. M., H. Steinberg, A. Yacoby, Y. Tserkovnyak, B. I. Halperin, K. W. Baldwin, L. N. Pfeiffer and K. W. West, "Spin-charge separation and localization in one dimension", Science **308**, 88 (2005).

Auslaender, O. M., A. Yacoby, R. de Picciotto, K. W. Baldwin, L. N. Pfeiffer and K. W. West, "Experimental evidence for resonant tunneling in a luttinger liquid", Phys. Rev. Lett. **84**, 1764 (2000).

Auslaender, O. M., A. Yacoby, R. de Picciotto, K. W. Baldwin, L. N. Pfeiffer and K. W. West, "Tunneling sepectroscopy of the elementary excitations in a one-dimensional wire", Science **295**, 825 (2002).

Blumenstein, C., J. Schäfer, S. Mietke, S. Meyer, A. Dollinger, M. Lochner, X. Y. Cui, L. Patthey, R. Matzdorf and R. Claessen, "Atomically controlled quantum chains hosting a tomonaga–luttinger liquid", Nature Physics **7**, 776 (2011).

Bockrath, M., D. H. Cobden, J. Lu, A. G. Rinzler, R. E. Smalley, L. Balents and P. L. McEuen, "Luttinger-liquid behaviour in carbon nanotubes", Nature **397**, 598 (1999).

Bokes, P. and R. W. Godby, "Conductance and polarization in quantum junctions", Phys. Rev. B **69**, 245420 (2004).

Boninsegni, N. V. P. M. and B. V. Svistunov, "Worm algorithm and diagrammatic monte carlo: A new approach to continuous-space path integral monte carlo simulations", Phys. Rev. E **74**, 036701 (2006).

Casula, M., S. Sorella and G. Senatore, "Ground state properties of the one-dimensional coulomb gas using the lattice regularized diffusion monte carlo method", Phys. Rev. B **74**, 245427 (2006).

Ceperley, D. M., "Path integral in the theory of condensed helium", Rev. Mod. Phys. **67**, 279 (1995).

Cheianov, V. V. and M. B. Zvonarev, "Nonunitary spin-charge separation in a one-dimensional fermion gas", Phys. Rev. Lett. **92**, 176401 (2004).

Chen, T. M., A. C. Graham, M. Pepper, F. Ffigakis, I. Farrer and D. A. Ritchie, "Odd-even spin effects and variation of g factor in a quasi-one-dimensional subband", Phys. Rev. B **79**, 081301 (2009).

Cho, A. Y., "Growth of periodic structures by the molecular beam method", Appl. Phys. Lett. **19**, 467 (1971).

Cronenwett, S. M., H. J. Lynch, D. Goldhaber-Gordon, L. P. Kouwenhoven, C. M. Marcus, K. Hirose, N. S. Wingreen and V. Umansky, "Low-temperature fate of the 0.7 structure in a point contact: A kondo-like correlated state in an open system", Phys. Rev. Lett. **88**, 226805 (2002).

Crook, R., A. C. Graham, C. G. Smith, I. Farrer, H. E. Beere and D. A. Ritchie, "Erasable electrostatic lithography for quantum components", Nature **424**, 751 (2003).

Crook, R., J. Prance, K. J. Thomas, S. J. Chorley, I. Farrer, D. A. Ritchie, M. Pepper and C. G. Smith, "Conductance quantization at a half-integer plateau in a symmetric gaas quantum wire", Science **312**, 1359 (2006).

de Picciotto, R., L. N. Pfeiffer, K. W. Baldwin and K. W. West, "Nonlinear response of a clean one-dimensional wire", Phys. Rev. Lett. **92**, 036805 (2004).

de Picciotto, R., H. L. Störmer, L. N. Pfeiffer, K. W. Baldwin and K. W. West, "Four-terminal resistance of a ballistic quantum wire", Nature **411**, 51 (2001).

Deshpande, V. V., M. Bockrath, L. I. Glazman and A. Yacoby, "Electron liquids and solids in one dimension", Nature **464**, 209 (2010).

Dingle, R., H. L. Störmer, A. C. Gossard and W. Wiegmann, "Electron mobilities in modulationdoped semiconductor heterojunction superlattice", Appl. Phys. Lett. **33**, 665 (1978).

Egger, R. and A. O. Gogolin, "Effective low-energy theory for correlated carbon nanotubes", Phys. Rev. Lett. **79**, 5082 (1997).

Feynman, R. P., *Statistical Mechanics* (Addison-Wesley, Reading, MA, 1972).

Fiete, G. A., "The spin-incoherent luttinger liquid", Rev. Mod. Phys. **79**, 801 (2007).

Fiete, G. A. and L. Balents, "Greens function for magnetically incoherent interacting electrons in one dimension", Phys. Rev. Lett. **93**, 226401 (2004).

Fiete, G. A., K. L. Hur and L. Balents, "Transport in a spin-incoherent luttinger liquid", Phys. Rev. B **72**, 125416 (2005a).

Fiete, G. A., J. Qian, Y. Tserkovnyak and B. I. Halperin, "Theory of momentum resolved tunneling into a short quantum wire", Phys. Rev. B **72**, 045315 (2005b).

Fogler, M. M. and E. Pivovarov, "Exchange interaction in quantum rings and wires in the wigner-crystal limit", Phys. Rev. B **72**, 195344 (2005).

Ghosal, A., A. D. Güçlü, C. J. Umrigar, D. Ullmo and H. U. Baranger, "Incipient wigner localization in circular quantum dots", Phys. Rev. B **76**, 085341 (2007).

Giamarchi, T., *Quantum Physics in One Dimension* (Clarendon, Oxford, 2004).

Girardeau, M., "Relationship between systems of impenetrable bosons and fermions in one dimension", J. Math. Phys. **1**, 516 (1960).

Giuliani, G. F. and G. Vignale, *Quantum Theory of the Electron Liquid* (Cambridge University Press, 2005).

Gréus, C., A. Forchel, J. Straka, K. Pieger and M. Emmerling, "Ingaas/gaas quantum wires defined by lateral top barrier modulation", Appl. Phys. Lett. **61**, 1199 (1992).

Güçlü, A. D., A. Ghosal, C. J. Umrigar and H. U. Baranger, "Interaction-induced strong localization in quantum dots", Phys. Rev. B **77**, 041301 (2008).

Güçlü, A. D., C. J. Umrigar, H. Jiang and H. U. Baranger, "Localization in an inhomogeneous quantum wire", Phys. Rev. B **80**, 201302 (2009).

Haldane, F. D. M., "'luttinger liquid theory' of one-dimensional quantum fluids. i. properties of the luttinger model and their extension to the general 1d interacting spinless fermi gas", J. Phys. C **14**, 2585 (1981).

Heidenreich, R., R. Seiler and D. A. Uhlenbrock, "The luttinger model", J. Stat. Phys. **22**, 27 (1980).

Hew, W. K., K. J. Thomas, M. Pepper, I. Farrer, D. Anderson, G. A. C. Jones and D. A. Ritchie, "Spin-incoherent transport in quantum wires", Phys. Rev. Lett. **101**, 036801 (2008).

Hew, W. K., K. J. Thomas, M. Pepper, I. Farrer, D. Anderson, G. A. C. Jones and D. A. Ritchie, "Incipient formation of an electron lattice in a weakly confined quantum wire", Phys. Rev. Lett. **102**, 056804 (2009).

Imambekov, A. and L. I. Glazman, "Universal theory of nonlinear luttinger liquid", Science **323**, 228 (2009).

Jamei, R., S. Kivelson and B. Spivak, "Universal aspects of coulomb-frustrated phase separation", Phys. Rev. Lett. **94**, 056805 (2005).

Jompol, Y., C. J. B. Ford, J. P. Griffiths, I. Farrer, G. A. C. Jones, D. Anderson, D. A. Ritchie, T. W. Silk and A. J. Schofield, "Probing spin-charge separation in a tomonaga-luttinger liquid", Science **325**, 597 (2009).

Kane, C., L. Balents and M. P. A. Fisher, "Coulomb interactions and mesoscopic effects in carbon nanotubes", Phys. Rev. Lett. **79**, 5086 (1997).

Klironomos, A. D., J. S. Meyer, T. Hikihara and K. A. Matveev, "Spin coupling in zigzag wigner crystals", Phys. Rev. B **76**, 075302 (2007).

Klironomos, A. D., R. R. Ramazashvili and K. A. Matveev, "Exchange coupling in a one-dimensional wigner crystal", Phys. Rev. B **72**, 195343 (2005).

Kristensen, A., H. Bruus, A. E. Hansen, J. B. Jensen, P. E. Lindelof, C. J. Marckmann, NewAuthor7, J. Nygård, C. B. Sørensen, F. Beuscher, A. Forchel and M. Michel, "Bias and temperature dependence of the 0.7 conductance anomaly in quantum point contacts", Phys. Rev. B **62**, 10950 (2000).

Kristensen, A., P. E. Lindelof, J. B. Jensen, M. Zaffalon, J. Hollingbery, S. W. Pedersen, J. Nygård, H. Bruus, S. M. Reimann, C. B. Sørensen, M. Michel and A. Forchel, "Temperature dependence of the "0.7" $2e^2/h$ quasi-plateau in strongly confined quantum point contacts", Physica B **249-251**, 180 (1998).

Kunets, V. P., C. S. Furrow, T. A. Morgan, Y. Hirono, W. M. E, V. G. Dorogan, Y. I. Mazur, V. P. Kunets and G. J. Salamo, "Ingaas quantum wire intermediate band solar cell", Appl. Phys. Lett. **101**, 041106 (2012).

Landauer, R., "Spatial variation of currents and fields due to scatterers in metallic conduction", IBM J. Res. Dev. **1**, 223 (1957).

Landauer, R., "Electrical resistance of disordered one-dimensional lattices", Phil. Mag. **21**, 863 (1970).

Lieb, E. and D. Mattis, "Theory of ferromagnetism and the ordering of electronic energy levels", Phys. Rev. **125**, 164 (1962).

Lieb, E. H. and W. Liniger, "Exact analysis of an interacting bose gas. the general solution and the ground state", pr **130**, 1605 (1963).

Luttinger, J. M., "An exactly soluble model of a many-fermion system", J. Math. Phys. **4**, 1154 (1963).

Maggs, A. C., "Multiscale monte carlo algorithm for simple fluids", Phys. Rev. Lett. **97**, 197802 (2006).

Massimo Boninsegni, N. P. and B. Svistunov, "Worm algorithm for continuous-space path integral monte carlo simulations", Phys. Rev. Lett. **96**, 070601 (2006).

Matveev, K. A., "Conductance of a quantum wire at low electron density", Phys. Rev. B **70**, 245319 (2004a).

Matveev, K. A., "Conductance of a quantum wire in the wigner-crystal regime", Phys. Rev. Lett. **92**, 106801 (2004b).

Matveev, K. A., A. Rurusaki and L. I. Glazman, "Asymmetric zero-bias anomaly for strongly interacting electrons in one dimension", Phys. Rev. Lett. **98**, 096403 (2007).

Meyer, J. S., K. A. Matveev and A. I. Larkin, "Transition from a one-dimensional to a quasi-one-dimensional state in interacting quantum wires", Phys. Rev. Lett. **98**, 126404 (2007).

Nightingale, M. P. and C. J. Umrigar, *Quantum Monte Carlo methods in physics and chemistry* (Kluwer Academic Publishers, 1999).

Patel, N. K., J. T. Nicholls, L. Martin-Moreno, M. Pepper, J. E. F. Frost, D. A. Ritchie and G. A. C. Jones, "Properties of a ballistic quasi-one-dimenstional constriction in a parallel high magnetic field", Phys. Rev. B **44**, 10973 (1991).

Pfeiffer, L., A. Yacoby, H. L. Störmer, K. L. Baldwin, J. Hasen, A. Pinczuk, W. Wegscheider and K. W. West, "Transport and optics in quantum wires fabricated by mbe overgrowth on the (110) cleaved edge", Microelectronics Journal **28**, 817 (1997).

Piacente, G., I. V. Schweigert, J. J. Betouras and F. M. Peeters, "Generic properties of a quasi-one-dimensional classical wigner crystal", Phys. Rev. B **69**, 045324 (2004).

Pollock, E. L., "The coulomb pair density matrix", Comp. Phys. Comm. **52**, 49 (1988).

Postma, H. W. Ch., M. de Jonge, Z. Yao and C. Dekker, "Electrical transport through carbon nanotube junctions created by mechanical manipulation", Phys. Rev. B **62**, R10653 (2000).

Rees, D. G., H. Totsuji and K. Kono, "Commensurability-dependent transport of a wigner crystal in a nanoconstriction", Phys. Rev. Lett. **108**, 176801 (2012).

Reynolds, P. J., D. M. Ceperley, B. J. Alder and W. A. Lester, "Fixed-node quantum monte carlo for molecules", J. Chem. Phys. **77**, 5593 (1982).

Shulenburger, L., M. Casula, G. Senatore and R. M. Martin, "Correlation effects in quasi-one-dimensional quantum wires", Phys. Rev. B **78**, 165303 (2008).

Smith, L. W., W. K. Hew, K. J. Thomas, M. Pepper, I. Farrer, D. Anderson, G. A. C. Jones and D. A. Ritchie, "Row coupling in an interacting quasi-one-dimensional quantum wire investigated using transport measurements", Phys. Rev. B **80**, 041306 (2009).

Steinberg, H., O. M. Auslaender, A. Yacoby, J. Qian, G. A. Fiete, Y. Tserkovnyak, B. I. Halperin, K. W. Baldwin, L. N. Pfeiffer and K. W. West, "Localization transition in a ballistic quantum wire", Phys. Rev. B **73**, 113307 (2006).

T.-M.Chen, A. M. I. D., "Bias-controlled spin polarization in quantum wires", Appl. Phys. Lett. **93**, 032102 (2008).

Temkin, H., G. J. Dolan, M. B. Panish and S. N. G. Chu, "Lowtemperature photoluminescence from ingaas/inp quantum wires and boxes", Appl. Phys. Lett. **50**, 413 (1987).

Thomas, K. J., J. T. Nicholls, N. J. Appleyard, M. Y. Simmons, M. Pepper, D. R. Mace, W. R. Tribe and D. A. Ritchie, "Interaction effects in a one-dimensional constriction", Phys. Rev. B **58**, 4846 (1998).

Thomas, K. J., J. T. Nicholls, M. Y. Simmons, M. Pepper, D. R. Mace and D. A. Ritchie, "Possible spin polarization in a one-dimensional electron gas", Phys. Rev. Lett. **77**, 135 (1996).

Thornton, T. J., M. Pepper, H. Ahmed, D. Andrews and G. J. Davies, "One-dimensional conduction in the 2d electron gas of a gaas-algaas heterojunction", Phys. Rev. Lett. **56**, 1198 (1986).

Timp, G., "Chapter 3: When does a wire become an electron waveguide", Semiconductors and Semimetals **35**, 113 (1992).

Tomonaga, S., "Remarks on bloch's method of sound waves applied to many-fermion problems", Prog. Theor. Phys. **5**, 544 (1950).

Trotter, H. F., "On the product of semi-groups of operators", Proc. Am. Math. Soc. **10**, 545 (1959).

Troyer, M., B. Ammon and E. Heeb, "Parallel object oriented monte carlo simulations", Lecture Notes in Computer Science **1505**, 191 (1998).

van Wees, B. J., L. P. Kouwenhoven, E. M. M. Willems, C. J. P. M. Harmans, J. E. Mooij, H. van Houten, C. W. J. Beenakker, J. G. Williamson and C. T. Foxon, "Quantum ballistic and adiabatic electron transport studied with quantum point contacts", Phys. Rev. B **43**, 12431 (1991).

Vieillefosse, P., "Coulomb pair density matrix 1", J. Stat. Phys. **74**, 1195 (1994a).

Vieillefosse, P., "Coulomb pair density matrix 2", J. Stat. Phys. **80**, 461 (1994b).

Wigner, E., "On the interactions of electrons in metals", Phys. Rev. **46**, 1002 (1934).

Yao, Z., H. W. Ch. Postma, L. Balents and C. Dekker, "Carbon nanotube intramolecular junctions", Nature **402**, 273 (1999).

Yoji Kunihashi, M. K. and J. Nitta, "Enhancement of spin lifetime in gate-fitted ingaas narrow wires", Phys. Rev. Lett. **102**, 226601 (2009).

Vita

Jianheng Liu was born on May 4, 1982 in Fujian, China. He received a B. S. in Physics from the University of Science and Technology of China in 2004 and a M. S. in Physics from the University of Science and Technology of China (USTC) in 2007. While in USTC, he worked with Prof. Tunan Ruan and Prof. Pengfei Zhang on the bound states of gluons. He began graduate study at the Arizona State University in the fall of 2007 on path integral Monte Carlo method with his advisor Prof. John Shumway.